NASA Technical Memorandum 112860
U. S. Army Research Laboratory Technical Report 1400

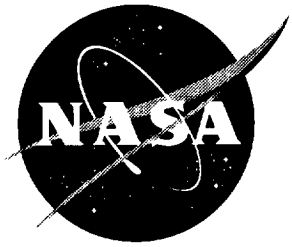

Fatigue Life Methodology for Tapered Composite Flexbeam Laminates

Gretchen B. Murri and T. Kevin O'Brien
Vehicle Technology Center
U.S. Army Research Laboratory
Langley Research Center, Hampton, Virginia

Carl Q. Rousseau
Bell Helicopter Textron, Fort Worth, Texas

May 1997

National Aeronautics and
Space Administration
Langley Research Center
Hampton, Virginia 23681-0001

ABSTRACT

The viability of a method for determining the fatigue life of composite rotor hub flexbeam laminates using delamination fatigue characterization data and a geometric non-linear finite element (FE) analysis was studied. Combined tension and bending loading was applied to non-linear tapered flexbeam laminates with internal ply drops. These laminates, consisting of coupon specimens cut from a full-size S2/E7T1 glass-epoxy flexbeam were tested in a hydraulic load frame under combined axial-tension and transverse cyclic bending loads. The magnitude of the axial load remained constant and the direction of the load rotated with the specimen as the cyclic bending load was applied. The first delamination damage observed in the specimens occurred at the area around the tip of the outermost ply-drop group. Subsequently, unstable delamination occurred by complete delamination along the length of the specimen. Continued cycling resulted in multiple delaminations. A 2D finite element model of the flexbeam was developed and a geometrically non-linear analysis was performed. The global responses of the model and test specimens agreed very well in terms of the transverse flexbeam tip-displacement and flapping angle. The FE model was used to calculate strain energy release rates (G) for delaminations initiating at the tip of the outer ply-drop area and growing toward the thick or thin regions of the flexbeam, as was observed in the specimens. The delamination growth toward the thick region was primarily mode II, whereas delamination growth toward the thin region was almost completely mode I. Material characterization data from cyclic double-cantilevered beam tests was used with the peak calculated G values to generate a curve predicting fatigue failure by unstable delamination as a function of the number of loading cycles. The calculated fatigue lives compared well with the test data.

NOMENCLATURE

c, d, e, f	curve fit constants in eqns. (1), (3), (4)
a	delamination length along taper above D4, mm
a'	delamination length along taper below D4, mm
b	delamination length toward thin region below B5, mm
E_1, E_2	Young's moduli in 1- and 2- directions, GPa
G	total strain energy release rate, J/m^2
G_{12}	shear moduli, GPa
G_I	mode I strain energy release rate, J/m^2
G_{Imax}	maximum mode I cyclic strain energy release rate, J/m^2
G_{II}	mode II strain energy release rate, J/m^2
h	measured ply thickness, mm
h'	prescribed ply thickness, mm
N	number of loading cycles
P	axial tension load, kN
t	ply-group thickness in FE model, mm
V	measured transverse (bending) load, kN
V'	prescribed transverse (bending) load, kN
v	transverse displacement at tip of flexbeam, mm
α	flexbeam taper angle, degrees
β	waviness angle, degrees
θ	laminate flapping angle, degrees
δ	transverse stroke of ATB test machine, mm
ε	flexbeam surface strain
ε_{max}	maximum cyclic surface strain
ν_{12}	Poisson's ratio

INTRODUCTION

Hingeless and bearingless helicopter rotor hubs are being designed using laminated composite materials to reduce weight, drag, and the number of parts. During flight, the rotor hub arm experiences centrifugal loads (CF) as well as bending in the flapping flexure region. In order to accommodate this bending, the stiffness of the flapping flexure region is changed by varying the thickness of the hub arm. This thickness change is accomplished by dropping, or terminating internal plies in that region. However, these internal ply-drop locations create discontinuities which are sources for delamination initiation [1-5]. In order to design damage resistant tapered structures, many parameters affecting delamination at dropped plies, such as the taper geometry and location of the ply-drops through the thickness must be considered [6-9].

Several studies have considered delamination failure in tapered laminates with internal ply drops under pure tension loads [1-14]. References 1-3, 6, 10, and 11 considered tapered laminates of a variety of different materials and with different internal ply-drop configurations. Both finite element (FE) modeling and stress-based failure criteria were used to predict the strength of the tapered laminates. In each study it was determined that delamination onset occurred at the ply-drops, as a results of high interlaminar stresses at those locations. Other investigators [4, 5, 7, 12-14] used a strain energy release rate approach to study delamination in tapered laminates subjected to axial tension loading. A two dimensional (2D) FE model developed in ref. 13 predicted that for a glass/epoxy laminate with three internal ply-drop steps, delamination will start at the junction of the thin and tapered regions, and will grow unstably into both the thin and tapered regions. Reference 7 showed that the strain energy release rate associated with a delamination growing from a ply-drop tip toward the thick section increases with increasing thickness of the discontinuous plies. In refs. 4, 5, and 14, strain energy release rate calculations from FE models were used with fracture toughness data to accurately predict delamination onset in unidirectional glass/epoxy and graphite/epoxy specimens.

Only a few studies so far have considered the effect of bending loads on tapered laminates. Reference 6 used a 3D FE model to study the effects of several ply-drop configuration parameters on interlaminar stresses in laminates with pure tension, bending, or torsion loads. Reference 15 investigated the possibility of controlling edge delamination by terminating a ply at a critical interface, a small distance from the free edge. Tension, bending and torsion loads were each applied to a 3D FE model. Terminating a -45° ply resulted in stress reductions at the free edge for tension and torsion loading, but not for bending. In ref. 16, the effect of combined tension and bending loading on a tapered laminate was studied using coupon specimens and a simple FE model composed of beam elements which were able to account for the effect of membrane loads on the flexural response of the laminate. The predicted surface strains from the FE analysis compared reasonably well with measured strains for laminates with both linear and nonlinear tapers.

In this study, the effect of combined tension-bending loading on glass-epoxy laminates with a nonlinear taper and internal ply-drops was studied. Coupon specimens cut from full-size flexbeams were subjected to a constant axial load and cyclic transverse bending load. For comparison with the test data, a 2D finite element model was developed which replicated the geometry and loading of the specimens. A geometrically nonlinear analysis was performed on the FE model.

EXPERIMENTS

Specimen Geometry and Test Conditions

In this study, six coupon specimens were cut from a full-size S2/E7T1 glass/epoxy flexbeam, as shown in fig. 1. The full-length beam was cut into two pieces crosswise, and then each half-beam was cut lengthwise into three 1-inch wide specimens. The specimens were then trimmed to a nominal length of 340 mm (13.4 inch). The specimens were symmetric about the midplane, and had a nonlinear taper design. The number of plies varied from 145 at the thick

end to 41 at the thin end. The flexbeam layup may be visualized as shown schematically in fig. 2, by assuming that the laminate consists of 5 continuous belt-ply groups (B), a continuous surface ply of woven 7781 E-glass/E7T1-2 fabric (F), and 4 dropped-ply groups (D) on each side of the mid-plane. Each dropped-ply group consisted of 13 plies of differing lengths, in a nonuniform staggered drop pattern, to produce the nonlinear surface contour. The continuous belt-ply groups are primarily composed of 0-degree laminae, and the dropped-ply groups are composed of 45-degree and -45-degree plies only. The material properties for S2/E7T1 and E-glass/E7T1-2 are given in Table 1. The ply-groups are labeled in fig. 2 as they are referred to later in this report. The lay-up for each ply-group is given in Table 2, where a bar over the ply-angle indicates a half-ply. Table 2 also gives the thicknesses of the continuous belt-ply groups and equivalent orthotropic properties calculated using laminated plate theory and assuming symmetry. The measured average ply thickness, h, was 0.203 mm (0.008 inch) for the tape material and 0.317 mm (0.0125 in) for the fabric layer.

Axial-Tension Bending Machine

Flexbeam specimens were tested in a servo-hydraulic load frame, called the Axial-Tension Bending (ATB) machine, which was designed and built to produce combined tension-bending loading (fig. 3). Because the axial load cell is located above the top grip, but below the pivot connecting the axial and transverse actuators, the tension load "rotates" with the specimen as the transverse load is applied. Hence, under axial load control, the magnitude of the tension load, P, remains constant as the specimen rotates under the transverse bending load, V, as shown in fig. 4. Therefore, with the axial tension load applied under load control and the bending applied using stroke control, a constant membrane load should be maintained throughout the loading cycle.

Static Tests

Prior to fatigue testing, the relationship between applied loads and specimen deflection and surface strains was determined by holding the axial load constant and incrementally increasing the transverse load. Specimens were first instrumented with strain gages at four locations along the length on each side: one near the junction of the thick and tapered regions, two in the tapered region, and one in the thin section. (See fig. 4.) The specimen was then clamped in the grips with the thick end in the fixed bottom grip. The gage length between the grips was 165 mm (6.5 inches). The specimen was placed in the fixture so that there was a 12.7 mm (0.5 inch) thick region, a 127 mm (5 inch) tapered region and a 25.4 mm (1 inch) thin region (fig. 4).

As fig. 4 shows, the specimen is mounted in the grips and the transverse load is applied at the pivot point, at a distance above the top grip, rather than at the top of the specimen. For static excursions, a constant axial tension load, P, of approximately 35.6 kN (8000 lbs.) was applied, and then the bending load, V, was applied, in steps, to produce a transverse stroke, δ, in increments of approximately 2.54 mm (0.1 inch), up to a maximum stroke of 30.5 mm (1.2 inch). At each transverse load step, the strains were recorded, as well as the transverse flexbeam tip-displacement, v, and flapping angle, θ (See fig. 4). The flexbeam tip-displacement was measured using a spring-loaded DCDT which was mounted to the side of the load frame and detected the displacement of a bracket attached to the centerline of the top grip. The flapping angle was measured by means of a digital protractor mounted to the top grip.

In ref. 16, the surface strains in a composite flexbeam specimen of S2/E773 material with a similar non-linear taper and the same dimensions were measured at four locations along the specimen length, with the flexbeam specimen subjected to combined tension and bending loading. Maximum strains always occurred on the tension-bending surface, in the tapered region, at approximately X=90.6 mm. It was assumed that the strain distribution in the current flexbeam specimens was similar. Therefore, peak surface strains measured at gage 3 (where

X=90.9 mm, 3.59 inch) in fig. 4 were plotted in fig. 5 as a function of applied transverse stroke, δ. The relationship is linear when the axial load is held constant.

Fatigue Tests

Because the ATB boundary conditions differed from those of the full-scale flexbeam in the hub, the fatigue tests were controlled to a desired maximum surface strain level, rather than a prescribed transverse deflection or flapping angle. Hence, the results shown in fig. 5 were used to select the maximum cyclic transverse stroke to apply corresponding to the desired maximum strain level (measured at gage 3). Prior to fatigue testing, the specimen edges were painted with a water soluble typewriter correction fluid which acts as a brittle coating and makes delaminations easier to see. Then the specimens were clamped in the grips and a tension load of approximately 35.6 kN (8000 lbs.) was applied. This axial load corresponds to the net axial stress due to CF tension in the full-scale hub. The maximum cyclic transverse load, V, in the fatigue test, was applied by cycling the load sinusoidally to the desired maximum transverse stroke at a frequency of 3 Hz, using fully-reversed loading (R=-1). The maximum strain always occurred on the tension-side of the applied bending load. Four of the six specimens were tested at a maximum cyclic surface strain, ε_{max}, of 11000 $\mu\varepsilon$, and the other two at ε_{max}=10000 $\mu\varepsilon$. The specimens were cycled until they either failed by unstable delamination completely along the length, or reached 2 million loading cycles without failing (considered a "runout").

FINITE ELEMENT ANALYSIS

Finite Element Model Geometry

A finite element model (FEM) of the tapered laminate was developed to duplicate, as closely as possible, the geometry of the tested flexbeams, including the non-linear taper in the specimen, and the boundary conditions of the ATB test configuration. A schematic of the

configuration to be modeled by FE is shown in fig. 6. The fixed-end of fig. 6 corresponds to the composite flexbeam, and the loaded-end is a continuous rectangular cross-section member that represents the upper grip and steel fixture connecting to the pivot point where the transverse load is applied, as shown in fig 4. In this way, by applying the axial tension and transverse loads to the free end of the model, the loading conditions of the model duplicate the test conditions.

The FE model was a 2D model and was geometrically symmetric about the midplane. However, because of the unsymmetric loading, the entire flexbeam was modeled. The continuous curvature of the tapered section of the flexbeam was approximated in the model by using ten short linear taper sections, each with gradually decreasing taper angles, from α=9.17° at X=12.7 mm (0.5 inch) in fig. 6 to α=0.0° at X=140 mm (5.5 inch). Continuous belt-ply-groups (B) and dropped-ply-groups (D) were modeled in the analysis, rather than each individual ply. Smeared orthotropic material properties calculated from laminated plate theory for each ply-group, assuming symmetry, were used to represent the different ply-groups. The Poisson ratio mismatch associated with this approach was assumed to be negligible because none of the ply-groups contained 90° plies. The smeared moduli in the global X-Y coordinate system, and thickness for each group are presented in Table 2. Because the bending stiffness of the steel fixtures was two orders of magnitude greater than the flexbeam [16], and to simplify the model, the elements at the thin-end that represent the steel loading fixtures were modeled with a rectangular cross-section equal to the thin end of the composite flexbeam, and were assigned moduli to yield a bending stiffness, EI, equivalent to the actual ATB fixtures.

Finite Element Mesh and Boundary Conditions

The FE model had 4960 nodes and 4144 four-noded isoparametric quadrilateral plane strain elements (see fig. 7). A 3-noded triangular element was used to represent a resin pocket at the

tip of each of the eight dropped-ply groups. The neat resin properties assigned to the resin elements are given in Table 1. Each distinct ply-group was modeled using one element through the ply-group thickness. The ply thickness in the model was h'=0.216 mm (0.0085 inch) for the tape plies and 0.324 mm (0.0128 inch) for the fabric. To facilitate accurate strain energy release rate analysis using the virtual crack closure technique (VCCT) [17], square elements were used in belt ply-groups B2, B3, B4, and B5, in the tapered region near the thick end of the model. Because the glass fibers were continuous in the belt-plies and followed the beam contour, a local coordinate system was defined for each element in the model, with the 1-direction parallel to the element side from node 1 to node 2 in the longitudinal direction . The local coordinate system was then used to define the material properties of each element. Because delamination was most often observed to occur first in the test specimens at the interfaces beneath ply-groups B5 and D4 (fig. 2), multi-point constraints (MPC) were imposed at those interfaces to allow simple modeling of delaminations by releasing the MPCs.

The nodes at the thick end of the model at X=0 were fixed in the X- and Y-directions to simulate clamped end conditions. An axial tension load of 35.6 kN (8000 lbs.) was applied at the thin end as a concentrated load. To produce bending, a point load of V'=4.45 kN (1000 lbs.) was applied in the negative Y-direction at the thin end of the model, corresponding to the pivot point in the ATB load frame, as shown in figs. 4 and 6.

Computation Methods

The ABAQUS finite element code was used in the analysis. Because the flexbeam undergoes large deflections, the geometric non-linear solution option was exercised. Also, as with the ATB load frame, the axial load in the model was able to "rotate" with the flexbeam as it deformed under the transverse load. The output from ABAQUS included nodal displacements, internal reaction forces at the nodes, and internal strains.

Nodal displacements and reaction forces were used along with the Virtual Crack Closure Technique (VCCT) to calculate strain energy release rates for the simulated delaminations. This technique calculates the mode I and mode II components of strain energy release rate (G_I and G_{II}, respectively), using the forces at the delamination tip, and the relative displacements behind the delamination tip, both measured in the local coordinate system; i.e., the normal-tangential (n-t) coordinate system for the deformed elements. Details of these calculations are given in refs. 17 and 18. The total strain energy release rate, G, is obtained by summing the individual mode components. Hence,

$$G = G_I + G_{II}$$

since $G_{III}=0$ for plane strain conditions.

RESULTS AND DISCUSSION

Global Response Comparison

Transverse displacements at the flexbeam tip, flapping angle, and surface strains in the FE model were compared to the test results to determine how accurately the model reproduced the global behavior of the test specimens under similar loading. In fig. 8, the measured surface strains from the four strain gage locations are compared to the ABAQUS calculated strains along the flexbeam length. The results shown are at the maximum transverse stroke condition (δ=30.5 mm (1.2 inch)) and with P=35.6 kN (8000 lbs.). Although the measured strains are somewhat higher than predicted at the location nearest the bottom grip, at the other three locations there is very good agreement between the test and analysis results.

Figure 9 shows the maximum surface strains vs. the flexbeam tip-displacement, as measured in the static excursion tests, along with the calculated results from the ABAQUS FE model. The agreement is very good throughout the range of tip-displacement, on both the tension-side and compression-side of the flexbeam. Figure 10 shows similar results for the

maximum strain vs. the flapping angle, from the static excursion tests and FE model. Based on these results, the FE model appears to duplicate the global response of the specimen under loading in the ATB very well.

Experimental Results

Throughout the fatigue loading cycle, the specimens were visually monitored periodically for delamination. The initial damage started as a tension crack at the interface between the D4 ply-group and the adjacent resin pocket on one side of the midplane, as shown schematically in fig. 11. Delaminations then grew from this crack toward the thick region, either at the interface under D4, indicated by delamination length *a* '; the interface above D4, indicated by delamination length *a*; or at both interfaces simultaneously, (see fig. 11). These delaminations were fairly uniform across the specimen width and grew rapidly, but in a stable manner, until they approached the juncture of the tapered and thick regions.

As the fatigue loading was continued, final unstable failure occurred by delaminations forming and growing unstably , along the entire length of the specimen from the tip of D4 into the thin region of the flexbeam, indicated by delamination length *b* in fig. 11. Figure 12 shows the number of cycles, N, to the initial visible delamination along *a* or *a*', and final unstable delamination failure along *b*. One specimen did not reach unstable delamination and was considered a runout at 2 million cycles (indicated by a right-pointing arrow on the data point in fig. 12). With continued loading, further unstable delaminations would initiate at ply-drop locations further outboard from the initial tension crack, but on the same side of the midplane, creating multiple delaminations.

Figure 13(a) shows a photo of a typical final failure. There are several delaminations along the length, including the longest one at the interface under B5. Figure 13(b) shows a close-up of the area around the tip of D4, where delaminations were first observed. The damage started as a tension crack between the resin pocket and dropped plies that initiated delaminations which

grew toward the thick region on both sides of the dropped section before any delamination was seen growing toward the thin region. In addition to visible delamination growth on the edges, three of the specimens sustained damage in the woven fabric surface ply (F). Splitting of the fabric started at the specimen edge, near the initial delamination site. Cracks grew across the specimen surface as the loading continued and delaminations grew from them in both directions, creating a visible delamination across the width of the specimen's surface, as shown in fig. 13(c).

Strain Energy Release Rate Calculations

The observed damage was created in the FE model by first modeling the tension crack between the tip of the dropped-ply group D4 and the adjacent resin pocket (see fig. 11). Then delaminations were simulated in the model by releasing pairs of multi-point constraints at the interfaces between D4 and B4, between D4 and B5, and between B4 and B5 (see inset in fig. 7). Strain energy release rates were calculated using VCCT for a delamination starting at the resin crack at the end of D4 and growing a distance a toward the thick region at the interface above D4 or a distance a' toward the thick region at the interface below D4. In addition, strain energy release rates were calculated for a delamination growing from the apex of the resin pocket in front of D4 a distance b toward the thin region at the interface between B4 and B5, (see figs. 2 and 11). The interfaces above and below the resin pocket element at D4 (see fig. 11) remained intact in the delaminated models.

The first G-values were calculated for a delamination of length a, with no other delaminations in the model (a'=0, b=0). The bottom curve on the left side of fig. 14 shows the results for this case. Initially, G is very small and increases very slowly until a=15.1 mm (0.593 inch), where the taper angle increases from 7.96° to 9.17°. At that point, as the delamination grows further in the thick direction, G increases more rapidly, and attains a maximum value when the delamination has grown all the way to the thick section at a=29.8 mm

(1.17 inch). The higher curve on the left of fig. 14 shows the G results assuming a delamination of length a' (under D4), with no other delaminations in the model (a=0, b=0). Again, G starts out with low values and increases slowly until a'=15 mm (0.59 inches). Then G increases very rapidly as the delamination is allowed to grow, reaching a peak at a'=29.5 mm (1.16 inch), just before the thick region. Figure 14 also shows that G is always higher for a delamination growing under D4, rather than over D4, making a delamination more likely to grow at that interface. Once a delamination forms along a' however, the magnitude of the peak G along a may rise, increasing the possibility that a delamination may form at the interface above D4 as well.

On the right side of fig. 14 are calculated G values for two cases of a delamination growing toward the thin region from the apex of the resin pocket ahead of D4. Because test results always showed delaminations existed at the interfaces above and below D4 before they started growing toward the thin region, the model was modified to contain delaminations of a=16.1 mm (0.635 inch) and a'=16 mm (0.631 inch) above and below D4. Then G was calculated for increasing values of b. The results are the bottom curve on the right in fig. 14. As the figure shows, G increases to a peak at b=30.9mm (1.22 inch), drops quickly, and then increases to a second (lower) peak at b=59.9 mm (2.36 inch). These calculations were repeated assuming that the delaminations above and below D4 extended all the way to the junction of the tapered and thick regions, i.e., a=30.8 mm (1.21 inch) and a'=30.6 mm (1.2 inch), and again letting a delamination grow a distance b toward the thin end. The results are the higher curve on the right of fig. 14. The initial G values are much higher for this case. This curve also increases rapidly to a peak at b=30.9 mm (1.22 inch) and drops, and reaches a second peak at b=51.2 mm (2.02 inch), similar to the lower curve. The test results and calculated G results in fig. 14 suggest that a delamination will grow first toward the thick region around D4, all the way to the junction of the tapered and thick regions. Once the interfaces above and below D4 are delaminated, a delamination will grow unstably along surface b.

The opening and shear components of G, (G_I and G_{II}, respectively), were calculated for all four modeled delamination configurations. Figure 15 shows G_{II}/G for the delamination growing toward the thick region. The figure shows that the delamination growth is always at least 70% mode II for both cases. For delamination along a, G_{II}/G drops from almost 100% at a=5.08 mm (0.2 inch), down to 70% at a=11.4 mm (0.45 inch), then increases to a peak at a=15.1 mm (0.593 inches) where the taper angle changes, drops again to 75%, and increases steadily back to 100%. For a delamination along a', G_{II}/G is fairly constant at about 95% until a'=15 mm (0.59 inches). Then there is a sudden drop. As the delamination grows further, G_{II}/G increases back to near 100%.

The behavior of both curves at the discreet change in taper angle (a=15.1 mm and a'=15 mm (0.593 and 0.59 inches)) is similar to results shown in ref. 19. In that study, the effect of fiber waviness on strain energy release rate was studied by modeling a delamination growing along an interface which changed from horizontal to an upward inclined ($-\beta$) or a downward inclined ($+\beta$) angle. Results of [19] showed that G_{II}/G increased as the waviness angle changed from the largest $+\beta$ values to the largest $-\beta$ values. These results can help explain the sudden local changes in mode ratios observed at the change in taper angle in the current model. Figure 16 shows an enlarged view of the FE mesh around D4. As the figure shows, at the interface above D4, at a=15.1 mm (0.593 inches), the taper angle increases from 7.96° to 9.17° ($-\beta$). However, on the interface below D4, at a'=15 mm (0.59 inches), there is also a small change in angle, but in the opposite direction, ($+\beta$). Referring to fig. 15, the $-\beta$ angle change along surface a resulted in a sudden increase in G_{II}/G at that location, whereas the $+\beta$ angle change along surface a', caused a sudden decrease in G_{II}/G.

Figure 17 shows the percentage of opening mode strain energy release rate (G_I/G) for the delamination growing toward the thin region. As the figure shows, for these delaminations, G was almost entirely mode I for both cases analyzed. However, the G_I/G ratio for the first case (with a=16.1 mm and a'=16 mm (0.635 and 0.631 inch)) shows small drops at b=11.7, 25.9, and 44.2 mm (0.46, 1.02, and 1.74 inch). There are taper angle changes at each of these locations, all in the -β direction, resulting in a temporary decrease in the percentage of G_I/G at each change. For the second case, where a=30.8 mm (1.21 inch) and a'=30.6 mm (1.2 inch), the effect of these changes is less pronounced, with a small drop at b=25.9 mm (1.02 inch), and a slightly larger drop at b=44.2 mm (1.74 inch), the location of the largest taper angle change.

Analyses of the relative percentages of G_I and G_{II} show that delamination growth along surfaces a or a' is predominantly mode II, but growth in the opposite direction along surface b is almost entirely mode I. In both cases, changing the taper angle, even by a small amount, in either a positive or negative direction, changes the ratios of G_I and G_{II} in the area near the angle change.

Failure Predictions

In refs. 4, 14 and 19, peak values of calculated strain energy release rates were used with material characterization data to predict delamination onset as a function of the number of loading cycles. Figure 18 presents G_{Imax} vs. N data from ref. 20 , for S2/E7T1 material. Each data point represents one double cantilevered beam (DCB) test specimen that was cycled until delamination onset was detected. A 5% change in DCB specimen compliance was used as the criteria for indicating delamination onset. Although delamination growth along surfaces a and a' was shown to be primarily mode II, previous studies have indicated that there may be little difference in mode I and mode II G vs. N data, especially at long lives [21]. For this

reason, and because G_{IImax} data was not available, the G_{Imax} values were used for all calculations. For the purpose of this study, a curve was fit through the data in fig. 18, and had the form

$$G_{Imax} = c\,(N^{d}) \tag{1}$$

where c=463 J/m^2 and d= -0.0816. Then, as in [4] , [14], and [19], it was assumed that delamination onset would occur in the flexbeams when the peak G from the FE analysis equaled the cyclic G_{Imax} at which delamination initiated in the DCB tests. That is, when

$$\left[\frac{Gh'}{V'^2}\right]_{FE} = \frac{G_{Imax}\,h}{V^2} \tag{2}$$

where the terms on the left side of the equation refer to G calculated for a flexbeam with an assumed ply thickness, h', subjected to a prescribed transverse load, V', in the FE model and on the right side, h is the measured average ply thickness for the flexbeam specimens and V is the bending load applied during testing. However, since the tests were conducted by operating at a chosen ε_{max} level, it is more useful to calculate a predicted curve of ε_{max} vs. N, for comparison with the test results. The static excursion tests showed that a linear relationship existed between the transverse load, V, and the surface strain, ε, as shown in fig. 19. The relationship between V and ε can be expressed as

$$\varepsilon = e + fV \tag{3}$$

where the intercept e=3.36e-3 and the slope f=1.335e-3 kN^{-1}. Equation (1) can be substituted into eq. (2) and rearranged to solve for the applied transverse load, V. Substituting the expression for V into eq. (3) gives

$$\varepsilon_{max}(N) = e + f\sqrt{\frac{c\,N^{d}h}{\left[\frac{Gh'}{V'^{2}}\right]_{FE}}} \qquad (4)$$

relating the number of loading cycles to the applied maximum surface strain.

The number of loading cycles to final unstable delamination, $N_{failure}$, can be considered as N_1, the number of cycles to the onset of delamination along a or a', plus N_2, the number of cycles for stable delamination growth along those interfaces, plus N_3, the number of additional cycles to the onset of unstable delamination along b, once a and a' have grown to the juncture with the thick region. If N_2 is considered negligible, then $N_{failure}$ can be approximated by $N_1 + N_3$. Equation (4) was used to calculate curves relating maximum cyclic strain and the number of loading cycles to the onset of delamination along a' (N_1), and to the onset of final unstable delamination (N_3).

Equation (4) was first computed for the case of a delamination growing from the tip of D4 toward the thick section (increasing a'), with no other delaminations (a=0, b=0) in the flexbeam, using the peak value of G_{FE}=98 J/m^2 (0.56 in-lb/in^2) from fig. 14. A curve relating the maximum cyclic strain to the number of loading cycles at delamination onset along a' (N_1) was calculated and is shown in fig. 20(a). A second curve was calculated, for a flexbeam with both interfaces around D4 completely delaminated (a=30.8 mm and a'=30.6 mm (1.21 and 1.2 inch)) and a delamination of length b growing toward the thin region. For this case the peak value of G_{FE}=126 J/m^2 (0.72 in-lb/in^2), from the right side of fig. 14, was used. The resulting curve, shown in fig. 20(b) relates the cyclic strain to the number of loading cycles at the onset of final unstable delamination (N_3). Adding the two curves in fig. 20 then results in a curve relating ε_{max} and N for final delamination failure. This curve is shown in fig. 21, along with the test results at unstable delamination.

The shaded area in fig. 21 represents the prediction, plus and minus one standard deviation. All the test data fall within one standard deviation of the prediction, although the tendency is to slightly under-predict the number of cycles to failure at the higher strain level, and slightly over-predict at the lower strain level.

CONCLUSIONS

Nonlinear tapered flexbeam laminates cut from a full-size composite rotor hub flexbeam were tested under combined axial tension and cyclic bending loads. The tension load remained constant while the cyclic transverse bending load was applied. The specimens failed by delaminations first starting around the tip of the outermost ply-drop group and growing toward the thick region of the flexbeam. Once the interfaces both above and below this dropped-ply group were delaminated, final failure occurred by unstable delamination growth into the thin region along the full length of the taper.

A 2D finite element model was developed which closely approximated the flexbeam geometry, boundary conditions, and loading. The model was analyzed using a geometrically nonlinear FE code. The FE model was able to accurately replicate the global response of the coupon specimens under the combined loading. Delaminations of various lengths were simulated in the model by releasing multipoint constraints (MPC) at the interfaces where delaminations were observed in the test specimens. Strain energy release rates (G) calculated using the virtual crack closure technique (VCCT) showed that:

(1) Delaminations originating at the tip of the outermost ply-drop group were more likely to grow at the interface under the dropped-plies than at the interface above the dropped ply group;

(2) Delaminations at either interface will grow until they extend all the way to the junction of the tapered and thin regions; and

(3) Once the interfaces around the dropped-ply group are delaminated, a delamination will grow unstably from the tip of the dropped-ply region toward the thin area of the flexbeam.

A comparison of the mode ratios for the different delaminations modeled showed that delamination growth toward the thick region was mostly Mode II, whereas delamination growth in the opposite direction was predominantly Mode I. The mode ratios were very sensitive to the discrete angle changes in the model. At locations where the taper changed in one direction, G_I/G decreased locally, and where the angle changed in the opposite direction, G_I/G increased locally.

Calculated peak G values were used with G_{Imax} vs. N data generated using DCB specimens to predict failure of the flexbeam specimens. The calculated fatigue life agrees well with the test data. The results indicate that using the calculated G values from a FE model, with delamination fatigue characterization data, is a viable method for determining the fatigue life of composite rotor hub flexbeam laminates.

REFERENCES

1. Fish, J. C. and Lee, S. W., "Tensile Strength of Tapered Composite Structures." AIAA Paper No. 88-2252, *Proceedings of the 30th AIAA/ASME/ASCE/AHS Structures, Structural Dynamics and Materials (SDM) Conference*, Williamsburg, VA, April 1988, pp. 324-333.
2. Hoa, S. V., Daoust, J., and Du, B. L., "Interlaminar Stresses in Tapered Laminates," *Polymer Composites*, Vol. 9, No. 5, October 1988, pp. 337-344.
3. Llanos, A. S., Lee, S. W., and Vizzini, A. J., "Delamination Prevention in Tapered Composite Structures under Uniaxial Tensile Loads," AIAA Paper No. 90-1063, *Proceedings of the 31st AIAA/ASME/ASCE/AHS Structures, Structural Dynamics and Materials (SDM) Conference*, Long Beach, CA, April 1990, pp. 1242-1252.
4. Murri, G. B., Salpekar, S. A., and O'Brien, T. K., "Fatigue Delamination Onset Prediction in Unidirectional Tapered Laminates," *Composite Materials: Fatigue and Fracture (Third Volume), ASTM STP 1110*, T. K. O'Brien, Ed., American Society for Testing and Materials, Philadelphia, 1991, pp. 312-339.
5. Wisnom, M. R., "Delamination in Tapered Unidirectional Glass Fibre-Epoxy Under Static Tension Loading," AIAA Paper No. 91-1142, *Proceedings of the 32nd AIAA/ASME/ASCE/AHS Structures, Structural Dynamics and Materials (SDM) Conference (Part 2)*, Baltimore, MD, April 1991, pp. 1162-1172.
6. Daoust, J. and Hoa, S. V., "Parameters Affecting Interlaminar Stresses in Tapered Laminates Under Static Loading Conditions," *Polymer Composites*, Vol. 10, No. 5, October 1989, pp. 374-383.
7. Trethewey, B. R., Jr; Gillespie, J. W., Jr; and Wilkins, D. J., "Interlaminar Performance of Tapered Composite Laminates," *Proceedings of the American Society for Composites, 5th Technical Conference*, East Lansing, MI, June 1990, pp. 361-372.

8. Botting, A. D., Vizzini, A. J., and Lee, S. W., "The Effect of Ply-Drop Configuration on the Delamination Strength of Tapered Composite Structures," *Proceedings of the AIAA/AHS/ASME/ASCE/ASC 33rd Structures, Structural Dynamics and Materials Conference*, Dallas, TX, Apr. 1992, pp. 40-47.

9. Fish, J. C. and Vizzini, A. J., "Delamination of Ply-Drop Configurations," *Composite Materials: Testing and Design (Eleventh Volume), ASTM STP 1206*, E. T. Camponeshi, Jr., Ed., American Society for Testing and Materials, Philadelphia, 1993, pp. 323-332.

10. Kemp, B. L. and Johnson, E. R., "Response and Failure Analysis of a Graphite-Epoxy Laminate Containing Terminating Internal Plies," AIAA Paper No. 85-0608, *Proceedings of the 26th AIAA/ASME/ASCE/AHS Structures, Structural Dynamics and Materials (SDM) Conference*, Orlando, FL, April 1985, pp. 13-24.

11. Curry, J. M., Johnson, E. R., and Starnes, J. H., "Effect of Dropped Plies on the Strength of Graphite-Epoxy Laminates," *Proceedings of the 29th AIAA/ASME/ASCE/-9AHS Structures, Structural Dynamics and Materials (SDM) Conference*, Monterey, CA, April 1987, pp. 737-747.

12. Armanios, E. A. and Parnas, L., "Delamination Analysis of Tapered Laminated Composites Under Tensile Loading," *Composite Materials: Fatigue and Fracture (Third Volume), ASTM STP 1110*, T. K. O'Brien, Ed., American Society for Testing and Materials, Philadelphia, 1991, pp. 340-358.

13. Salpekar, S. A., Raju, I. S., and O'Brien, T. K., "Strain Energy Release Rate Analysis of Delamination in a Tapered Laminate Subjected to Tension Load," *Proceedings of the American Society for Composites, Third Technical Conference*, Seattle, WA, Sept. 1988, pp. 642-654.

14. Murri, G. B., O'Brien, T. K., and Salpekar, S. A., "Tension Fatigue of Glass/Epoxy and Graphite/Epoxy Tapered Laminates," *Journal of the American Helicopter Society*, Vol. 38, No. 1, Jan. 1993, pp. 29-37.

15. Ochoa, O. O. and Chan, W. S., "Tapered Laminates: A Study on Delamination Characterization," *Proceedings of the American Society for Composites, 3rd Technical Conference*, Seattle, WA, September 1988, pp. 633-641.

16. O'Brien, T. K., Murri, G. B., Hagemeier, R., and Rogers, C., "Combined Tension and Bending Testing of Tapered Composite Laminates," *Applied Composite Materials*, Vol. 1, No. 6, 1995, pp. 401-413.

17. Rybicki, E. F., and Kanninen, M. F., "A Finite Element Calculation of Stress-Intensity Factors by a Modified Crack-Closure Integral," *Engineering Fracture Mechanics*, Vol. 9, 1977, pp. 931-938.

18. Raju, I. S., "Simple Formulas for Strain-Energy Release Rates with Higher Order and Singular Finite Elements," NASA Contractor Report 178186, December 1986.

19. Li, J., and O'Brien, T. K., "Ply Waviness Effects on the Pull-off Loads in Composite Hat Stringer Specimens," *Proceedings of the 14th U.S. Army Symposium on Solid Mechanics*, Myrtle Beach, SC, October 16-18, 1996.

20. Martin, R. H., "Accelerated Methods for the Determination of Long Term Fatigue Properties of Glass Reinforced Plastics for Rotorcraft Applications," Materials Engineering Research Laboratory (MERL), Report No. N68171-96-C-9061, London, August 1996.

21. Martin, R. H., and Murri, G. B., "Characterization of Mode I and Mode II Delamination Growth and Thresholds in AS4/PEEK Composites," Composite Materials: Testing and Design (Ninth Volume), ASTM STP 1059, S. P. Garbo, Ed., American Society for Testing and Materials, Philadelphia, 1990, pp. 251-270.

22. Shivakumar, K. N. and Crews, J. H., Jr., "Bolt Clampup Relaxation in Graphite/Epoxy Laminate," Long Term Behavior of Composites, ASTM STP 813, T. K. O'Brien, Ed., American Society for Testing and Materials, Philadelphia, 1983, pp. 5-22.

Table 1. Material Properties

Material	E_{11}, GPa	E_{22}, GPa	G_{12}, GPa	ν_{12}
S2/E7T1 tape	47.6	12.6	4.81	0.28
E-glass/E7T1-2 fabric	25.3	24.1	4.56	0.153
Steel	201	201	77.3	0.30
Neat resin[22]	4.10	4.10	1.54	0.33

Table 2. Ply-Group Layups and Smeared Properties

Ply Group	Layup	E_{xx}, GPa	E_{yy}, GPa	G_{xy}, GPa	ν_{xy}	t, mm
B1	$[0_2/\overline{45}]$	41.1	13. 7	6.32	0.34	0.54
B2, B4, B5	$[0_4]$	47.6	12.6	4.81	0.28	0.864
B3	$[\pm 45/0_2]$	31.6	15.6	9.19	0.33	0.864
F	woven ±45	25.3	24.1	4.56	0.15	0.305
D1, D2, D3, D4	$[\pm 45]_n$	4.10	4.10	1.54	0.33	2.81*

* at thickest point

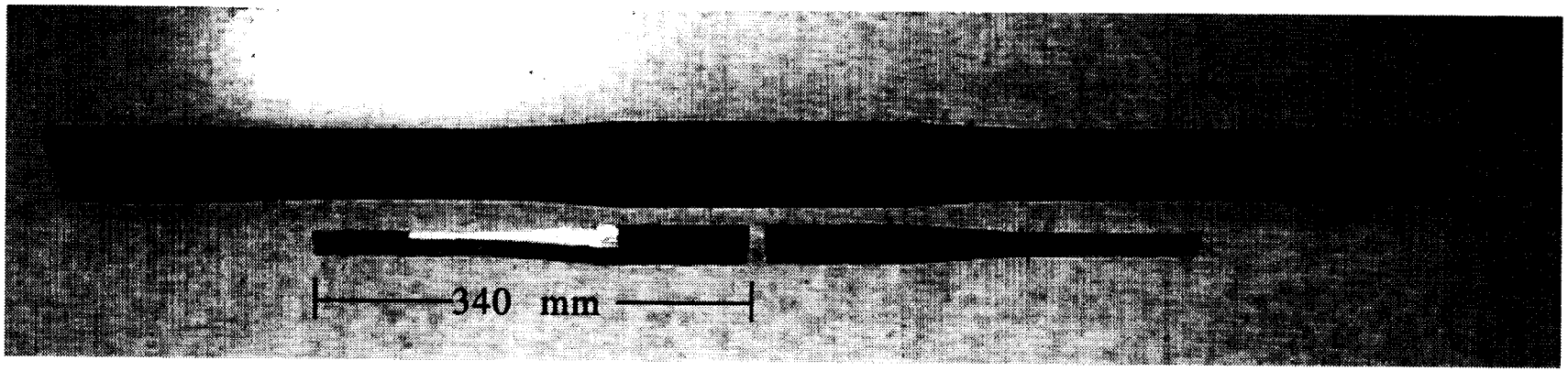

Figure 1. Full-scale flexbeam and coupon test specimens.

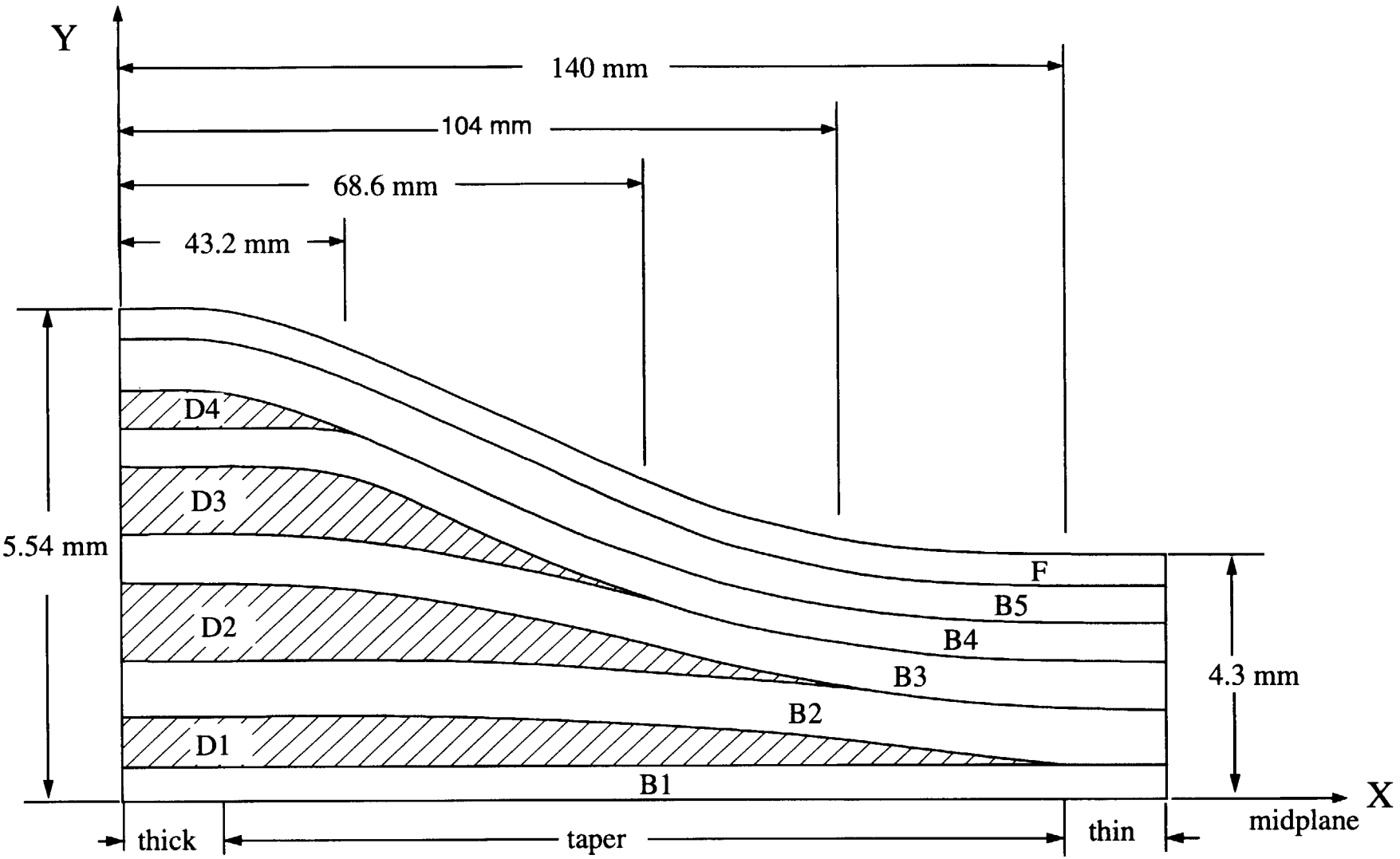

Note: Drawing not to scale

Figure 2. Schematic of half-laminate with plygroup labels.

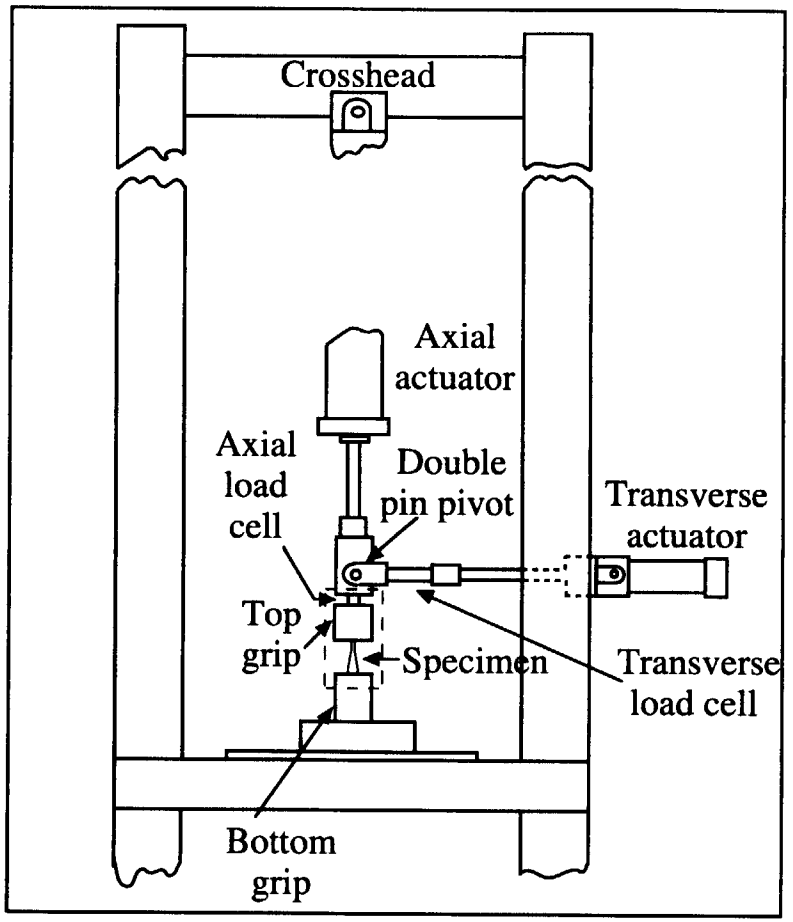

(a) schematic

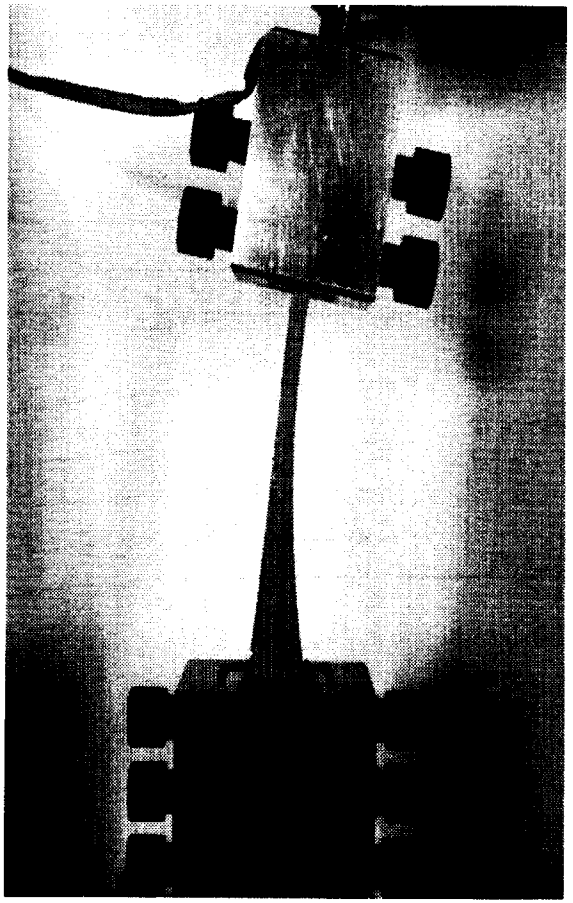

(b) deformed specimen

Figure 3. Axial tension and bending test stand and deformed flexbeam.

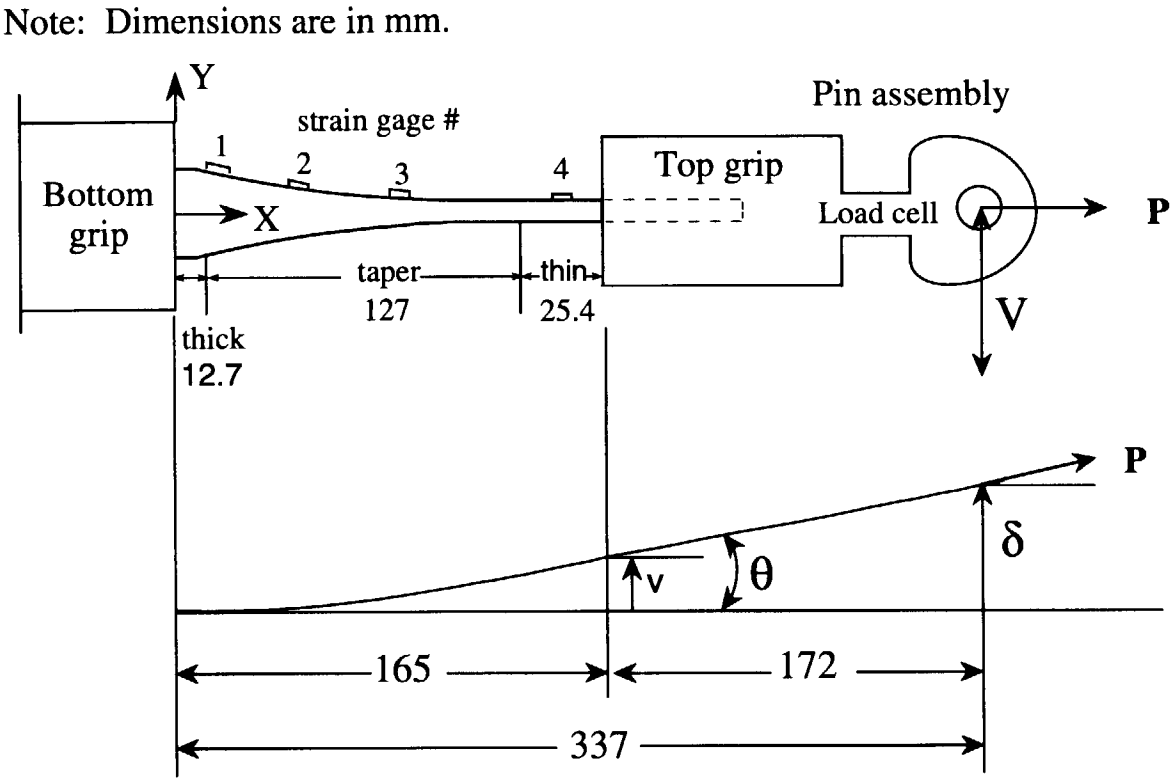

Figure 4. Test specimen and loading fixtures with combined loading.

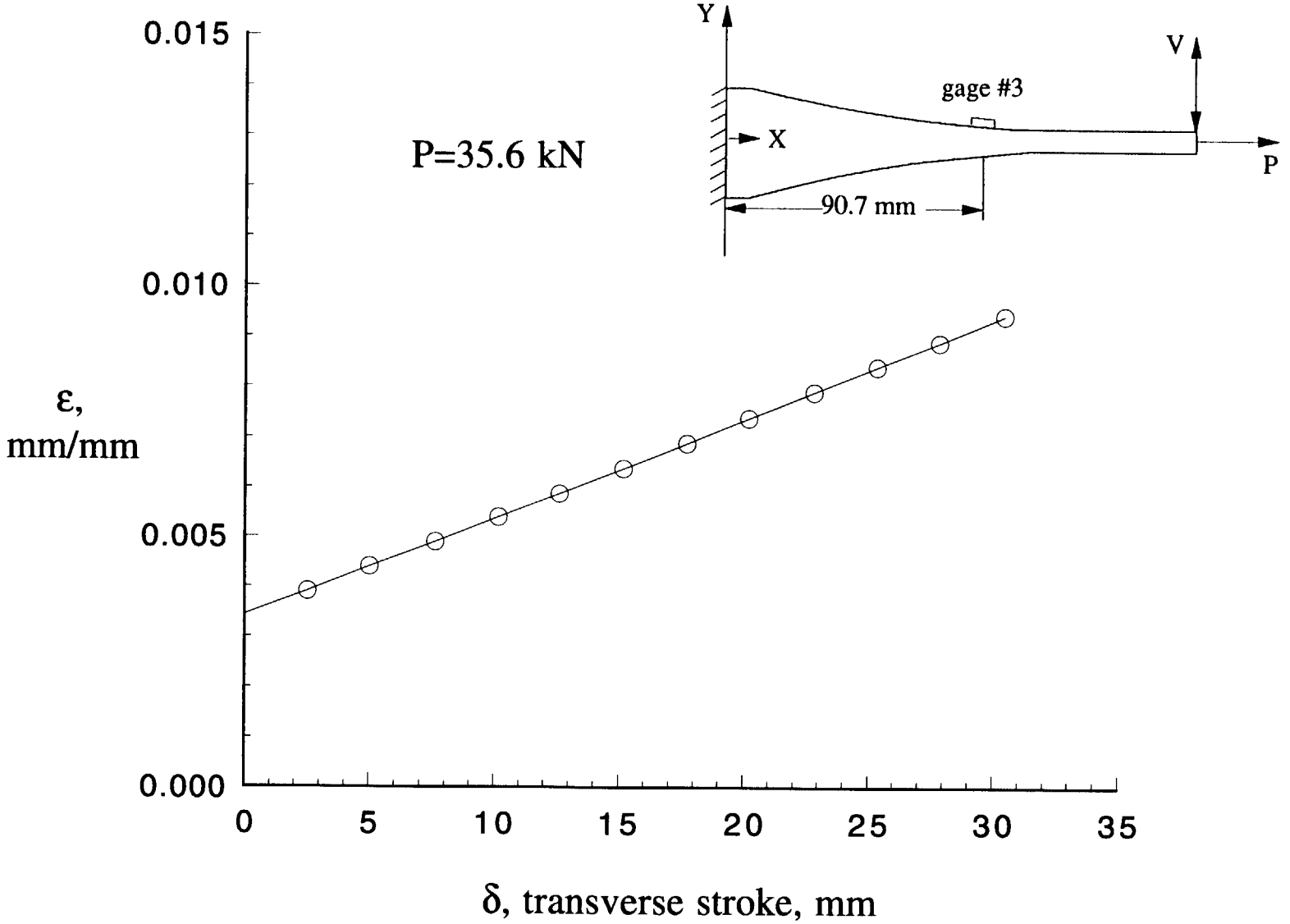

Figure 5. Transverse stroke-peak surface strain response of nonlinear tapered flexbeam in the Axial Tension and Bending (ATB) load frame.

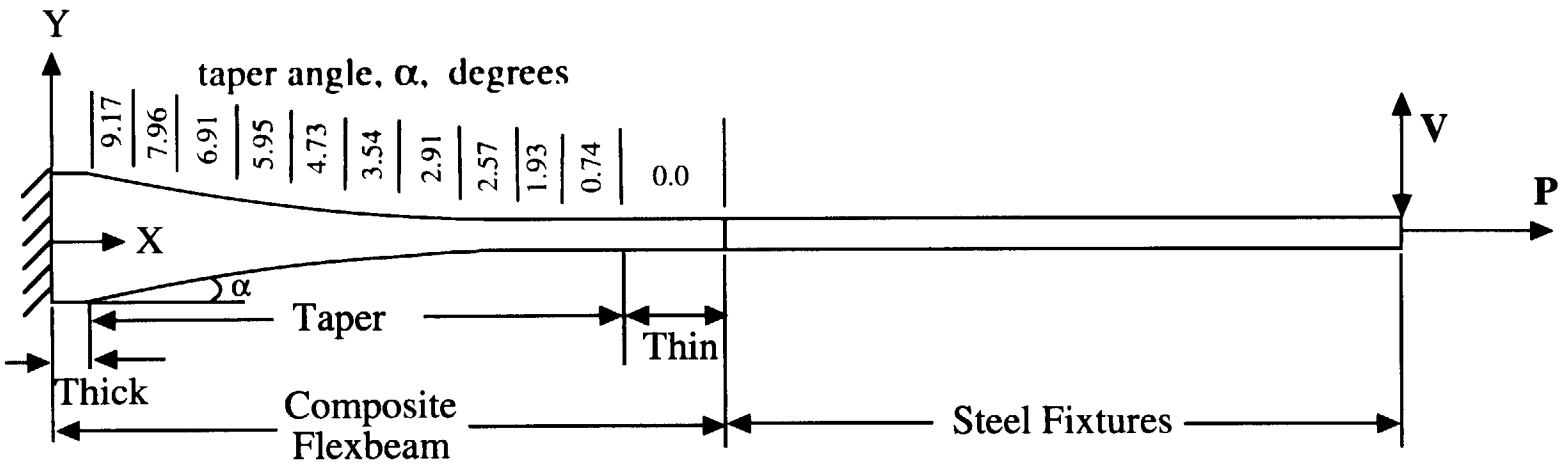

Figure 6. Nonlinear tapered flexbeam model with discreet taper angles and combined loading.

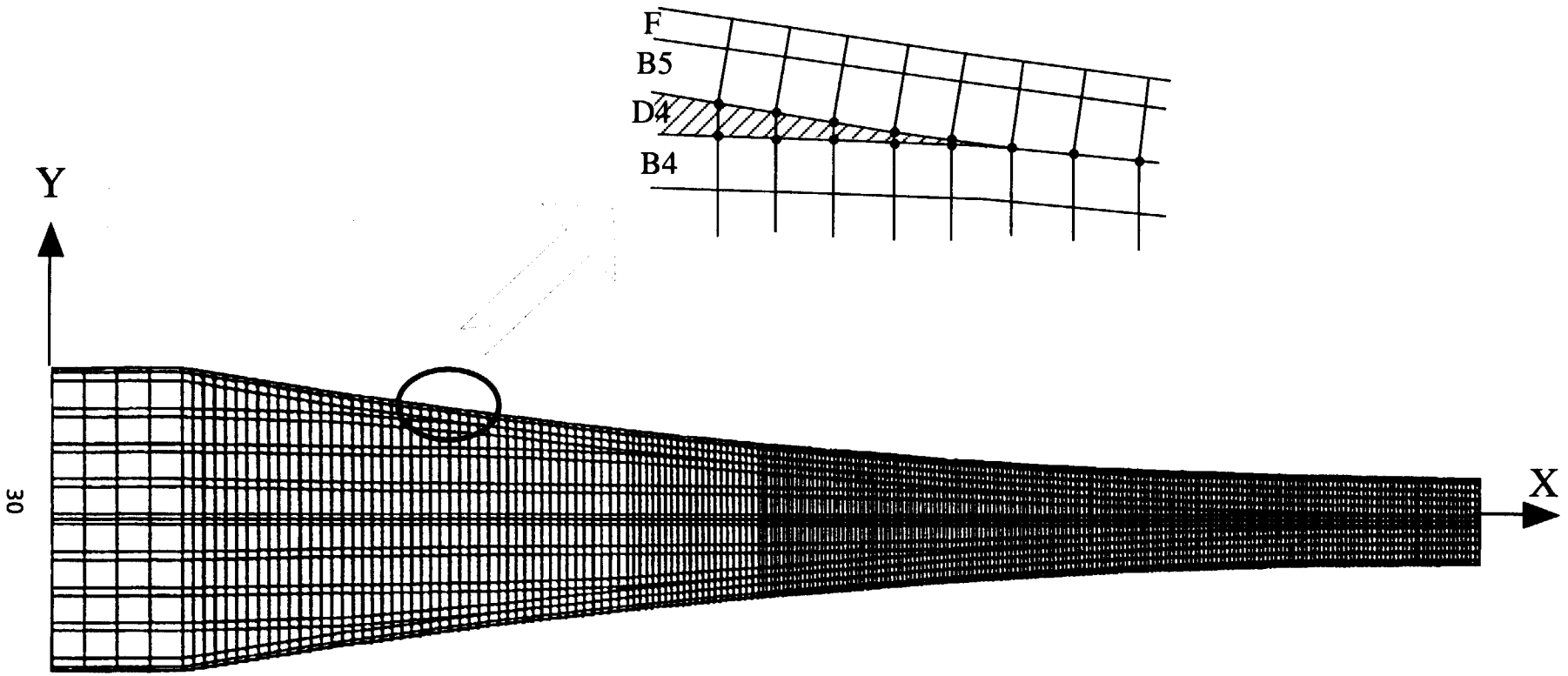

Figure 7. Finite element mesh of nonlinear tapered flexbeam laminate.

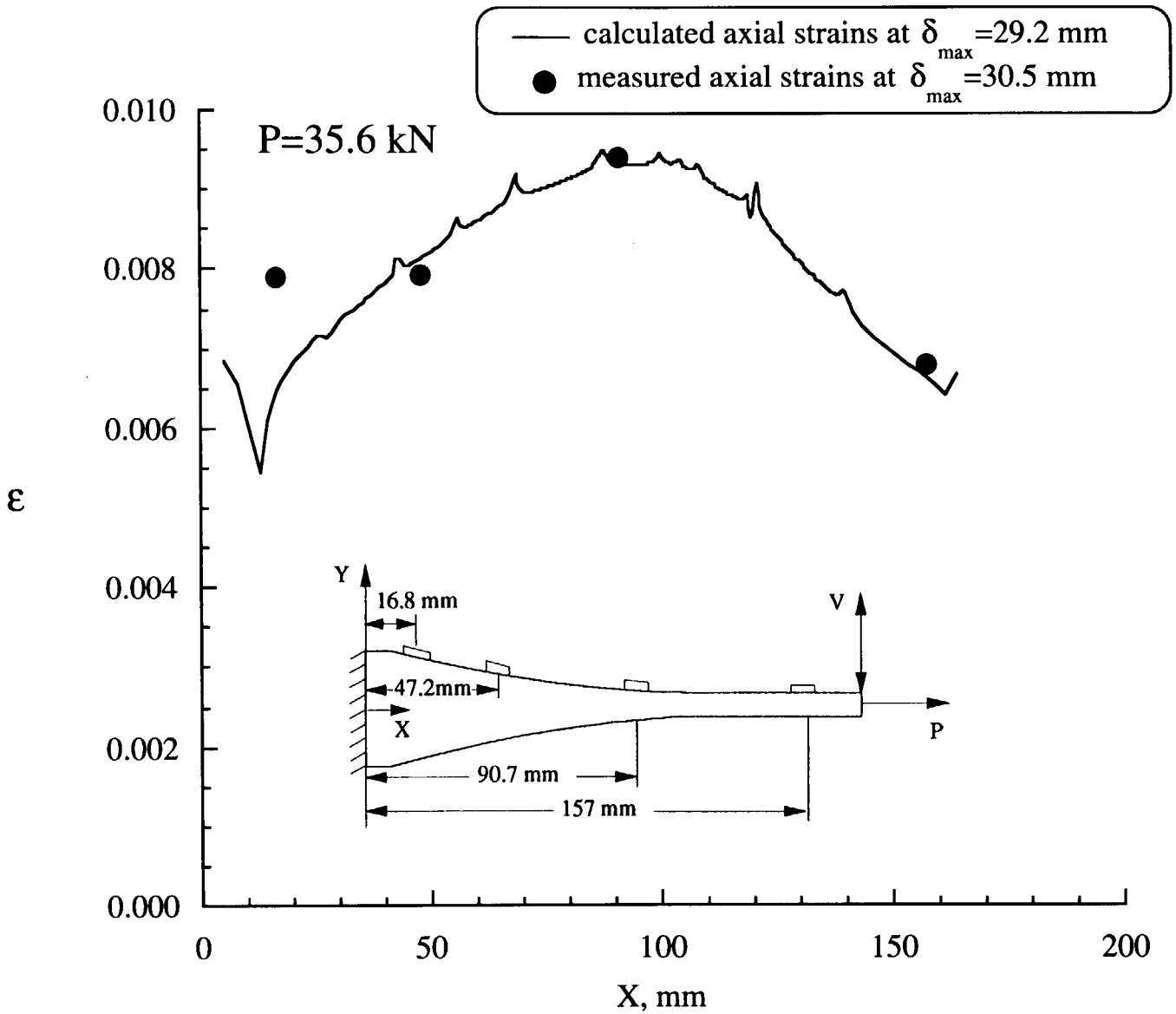

Figure 8. Surface strains in nonlinear tapered flexbeam with combined tension and bending loading.

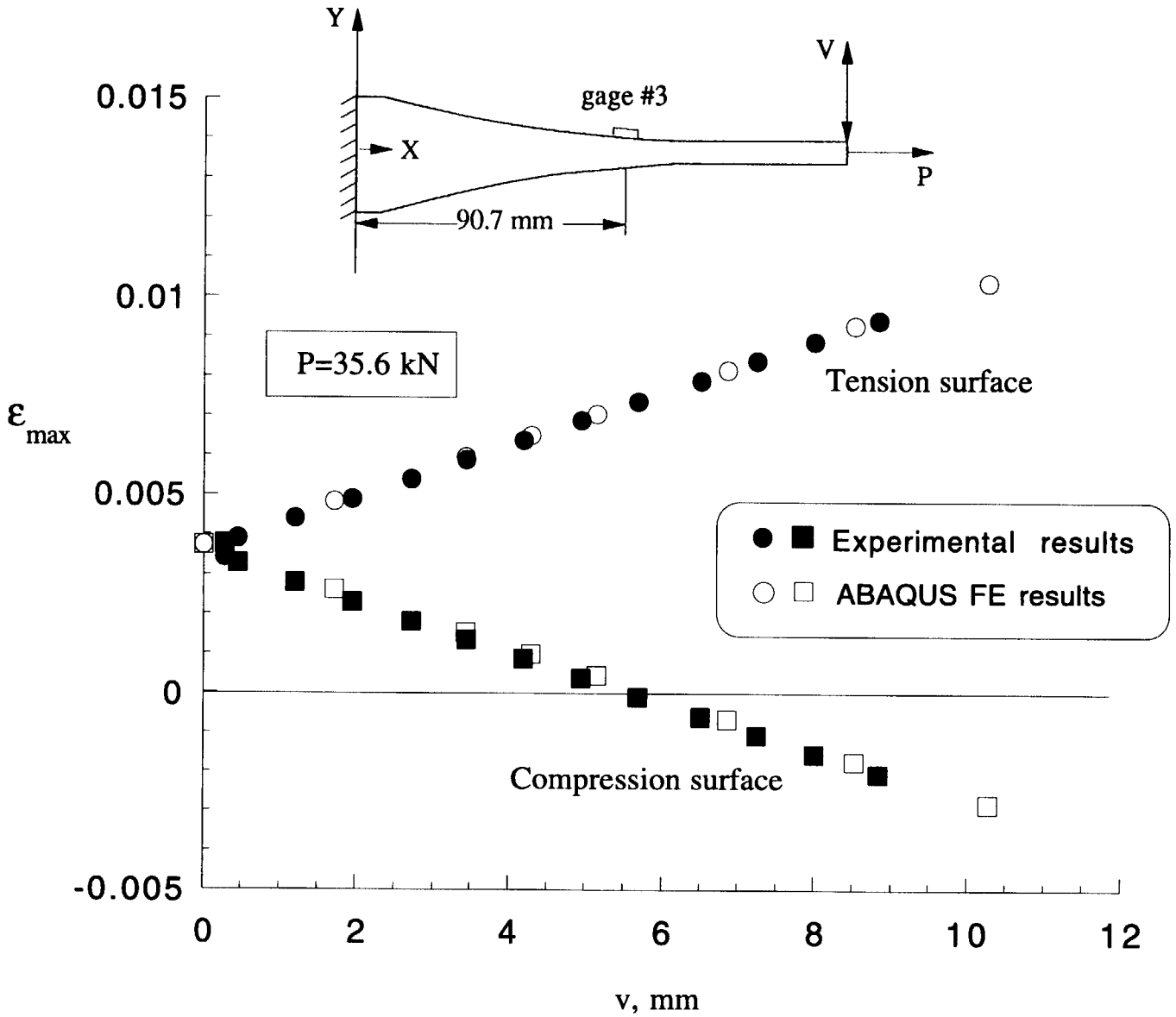

Figure 9. Calculated and measured surface strains vs. flexbeam tip-displacement, v, in nonlinear tapered flexbeam laminate.

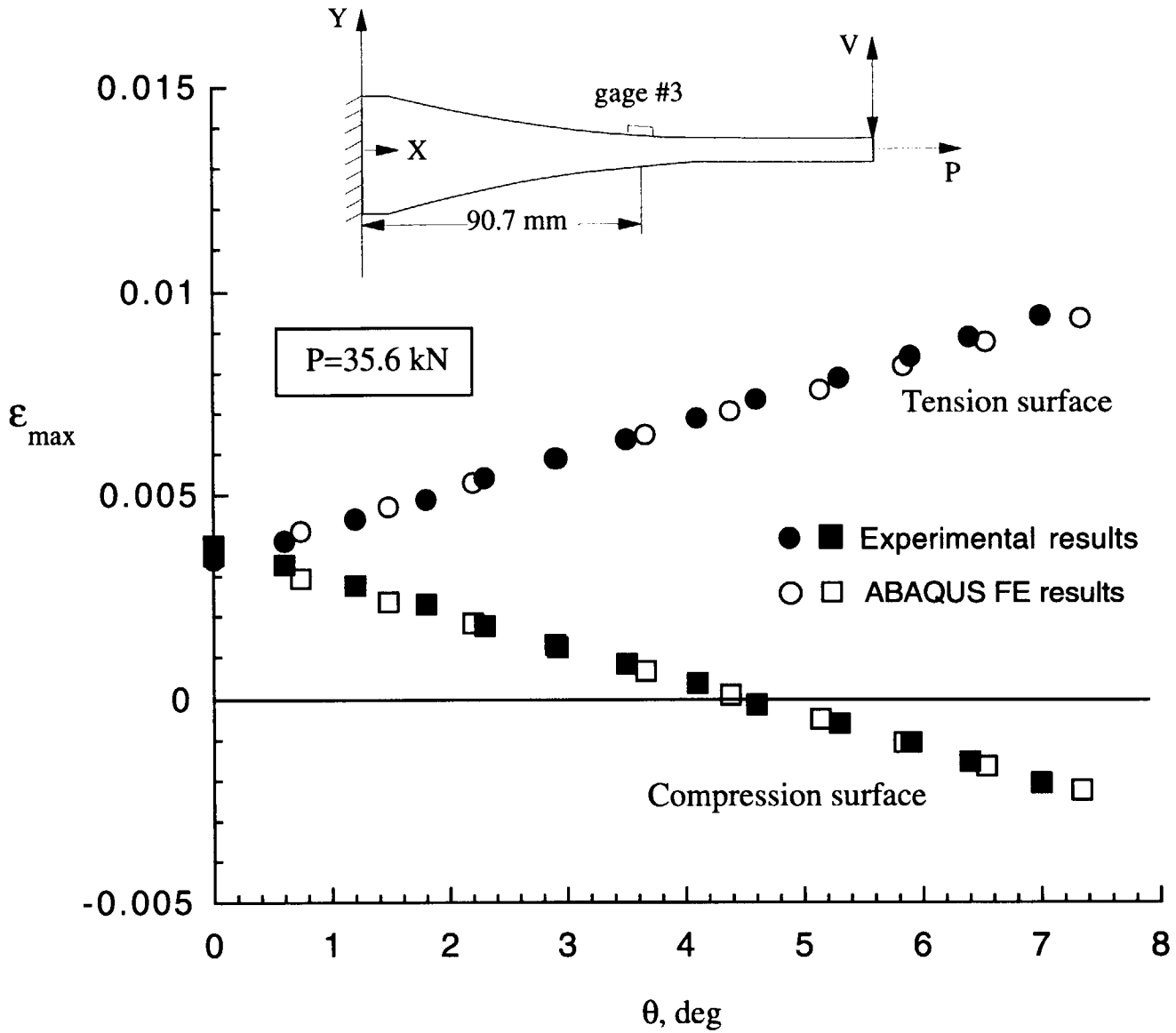

Figure 10. Calculated and measured surface strains vs. flapping angle, θ, in nonlinear tapered flexbeam laminate.

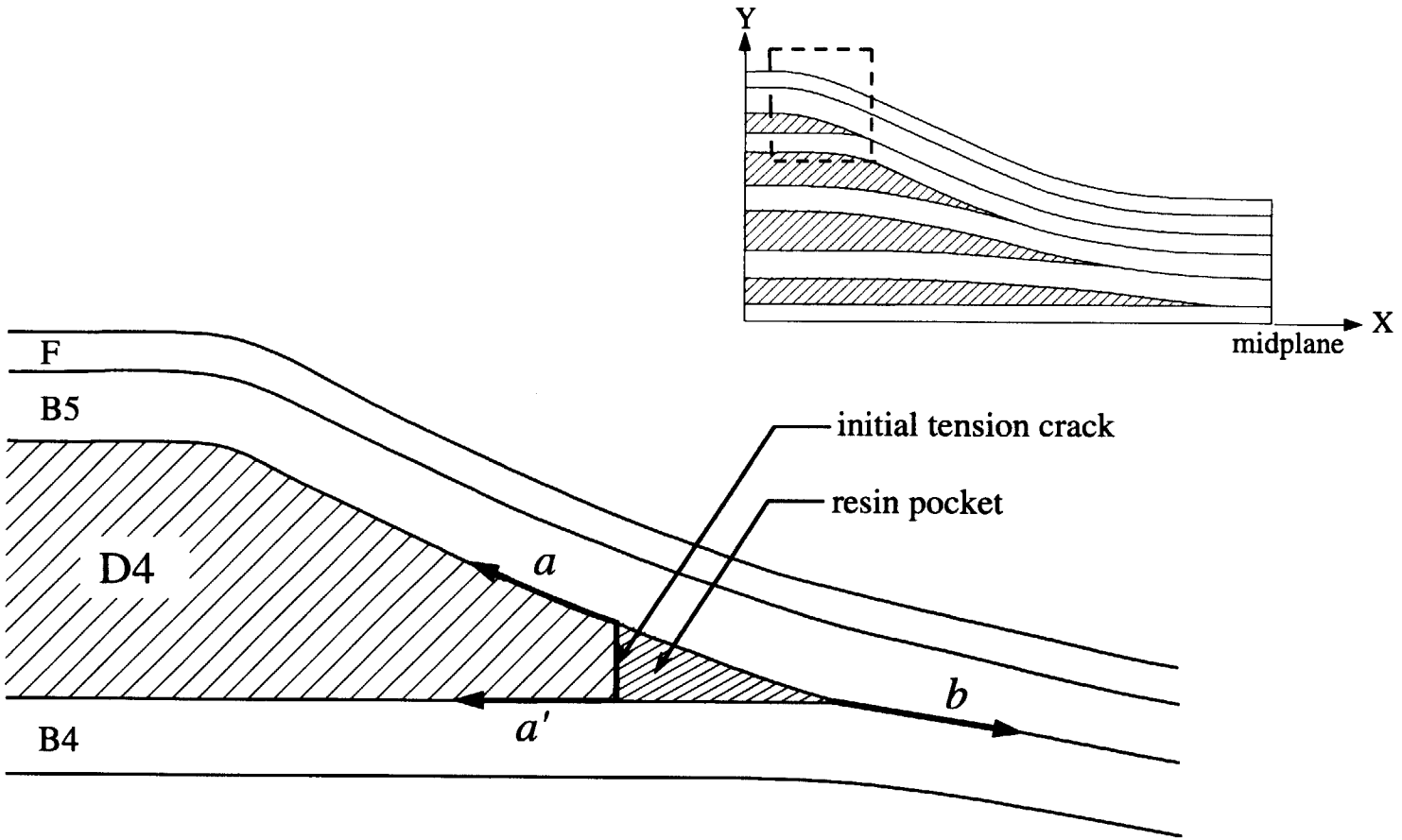

Note: Drawing not to scale.

Figure 11. Delamination starting at tip of ply group D4.

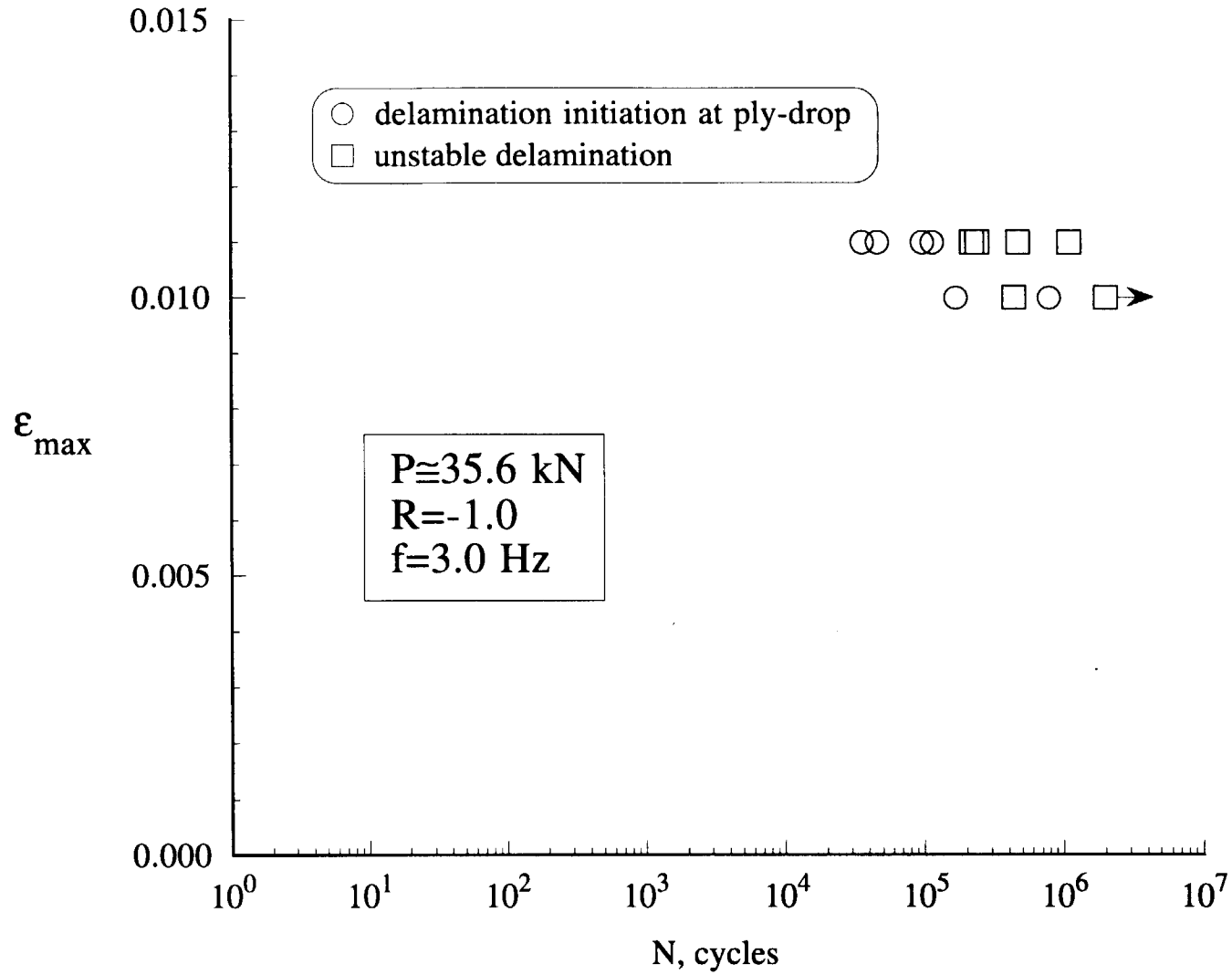

Figure 12. Fatigue delamination response in composite flexbeam specimens under combined tension and bending loading.

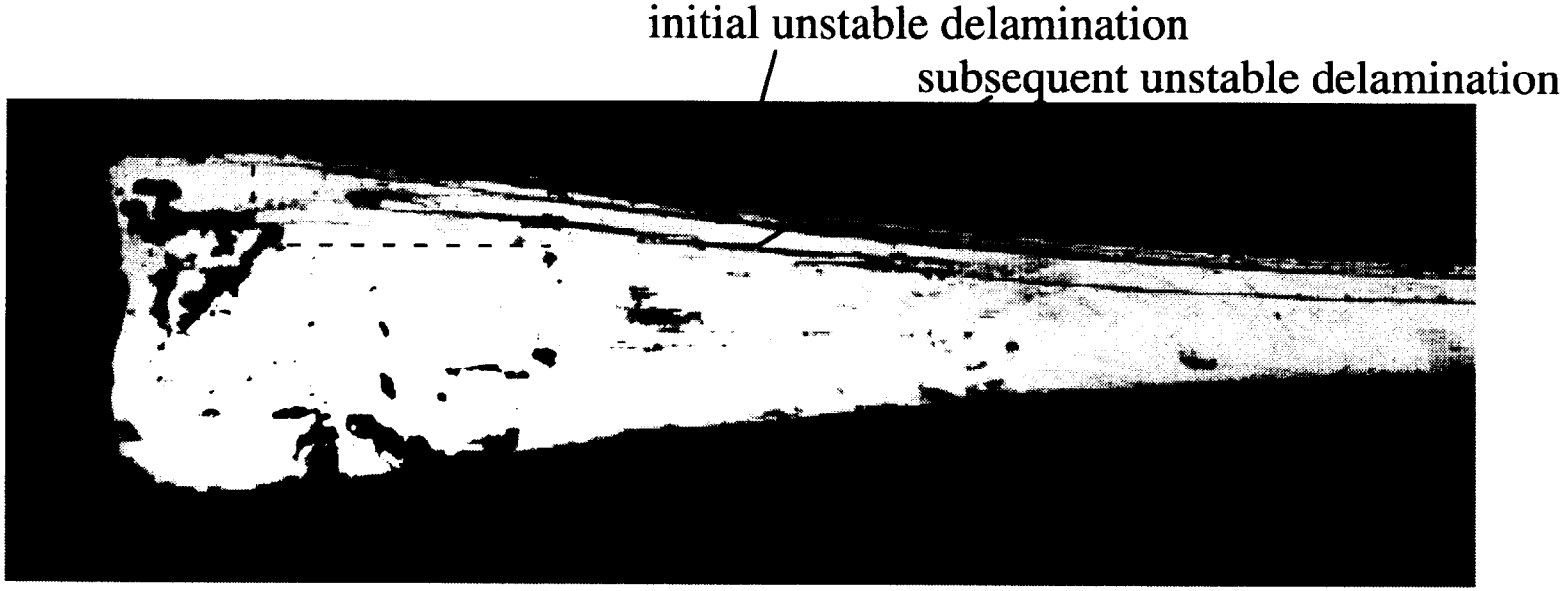

(a) final failure with multiple delaminations

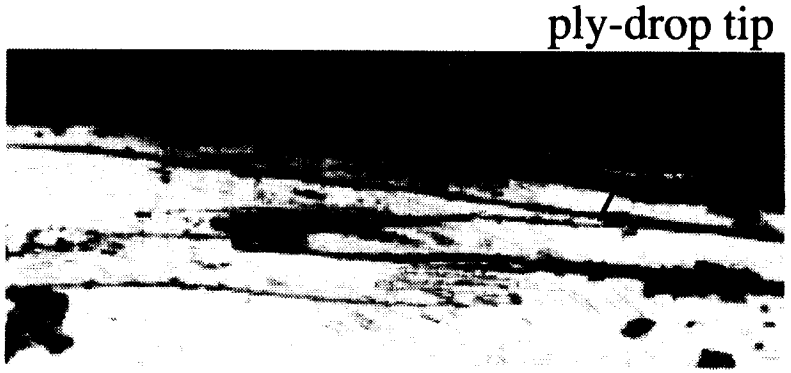

(b) initial damage at ply-drop and associated delamination

(c) damage in surface fabric layer

Figure 13. Flexbeam test specimen with delamination damage.

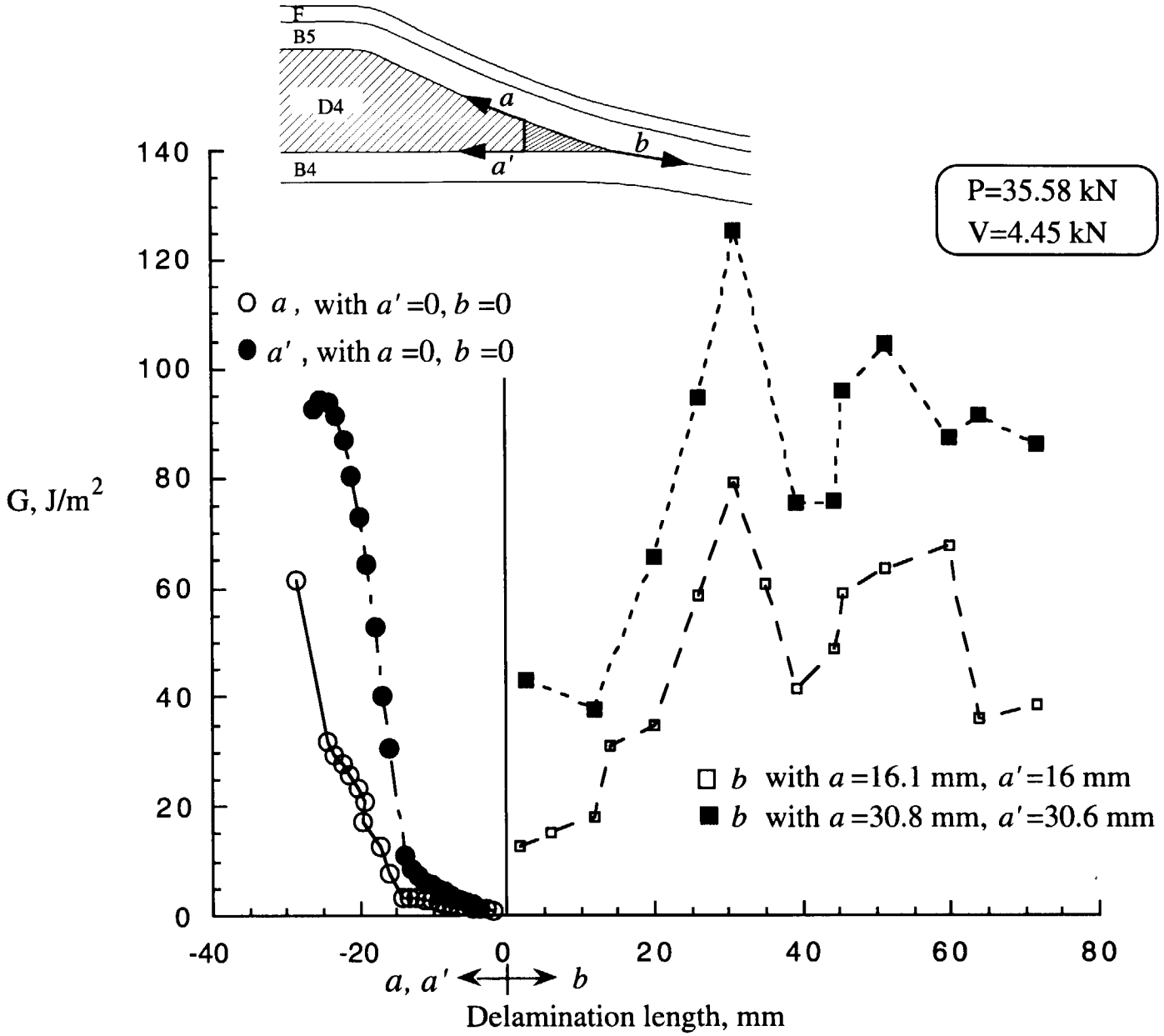

Figure 14. Strain energy release rates for delamination growth in nonlinear tapered laminates under combined tension and bending loading.

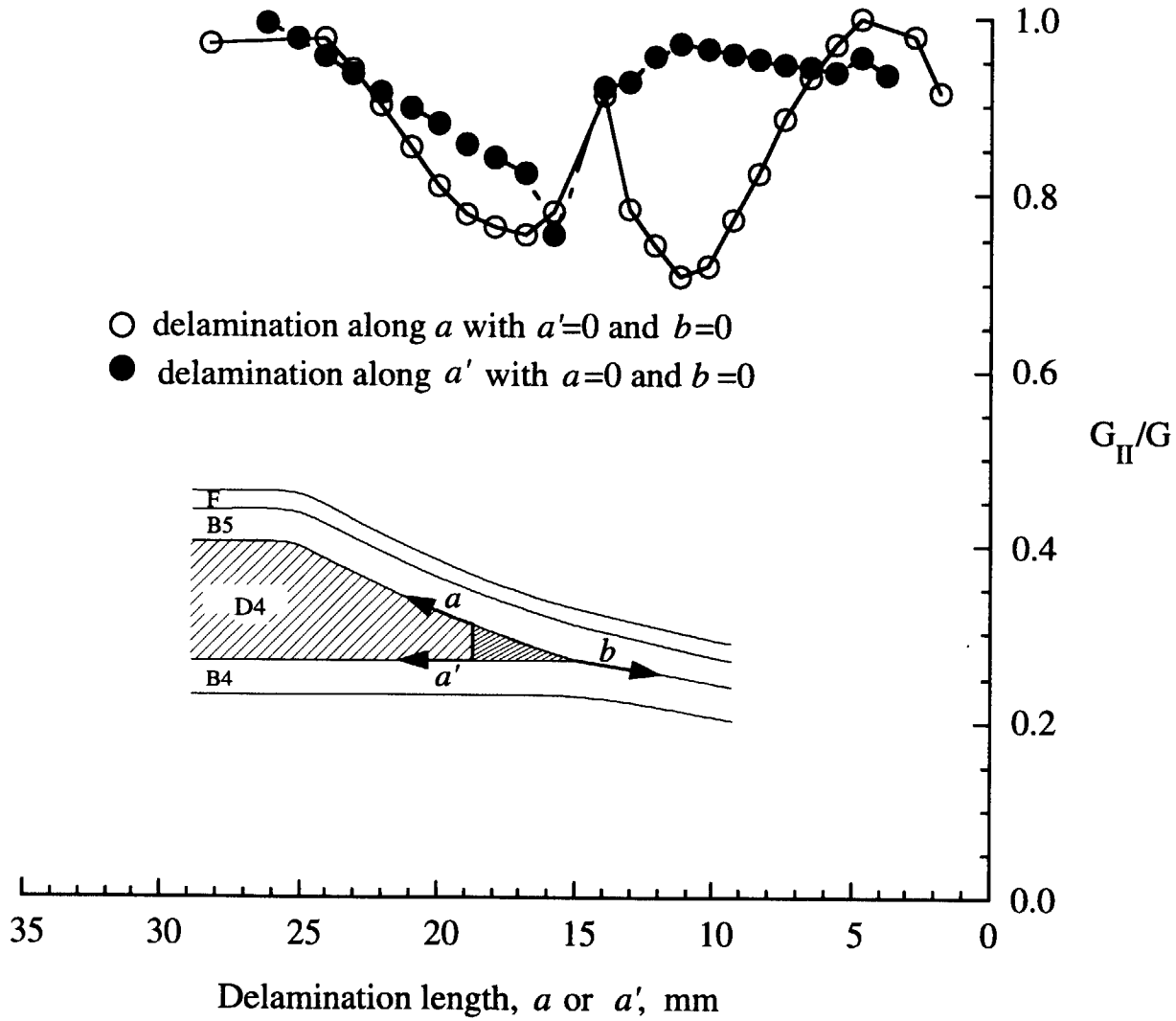

Figure 15. G_{II}/G ratio for delamination around ply-group D4.

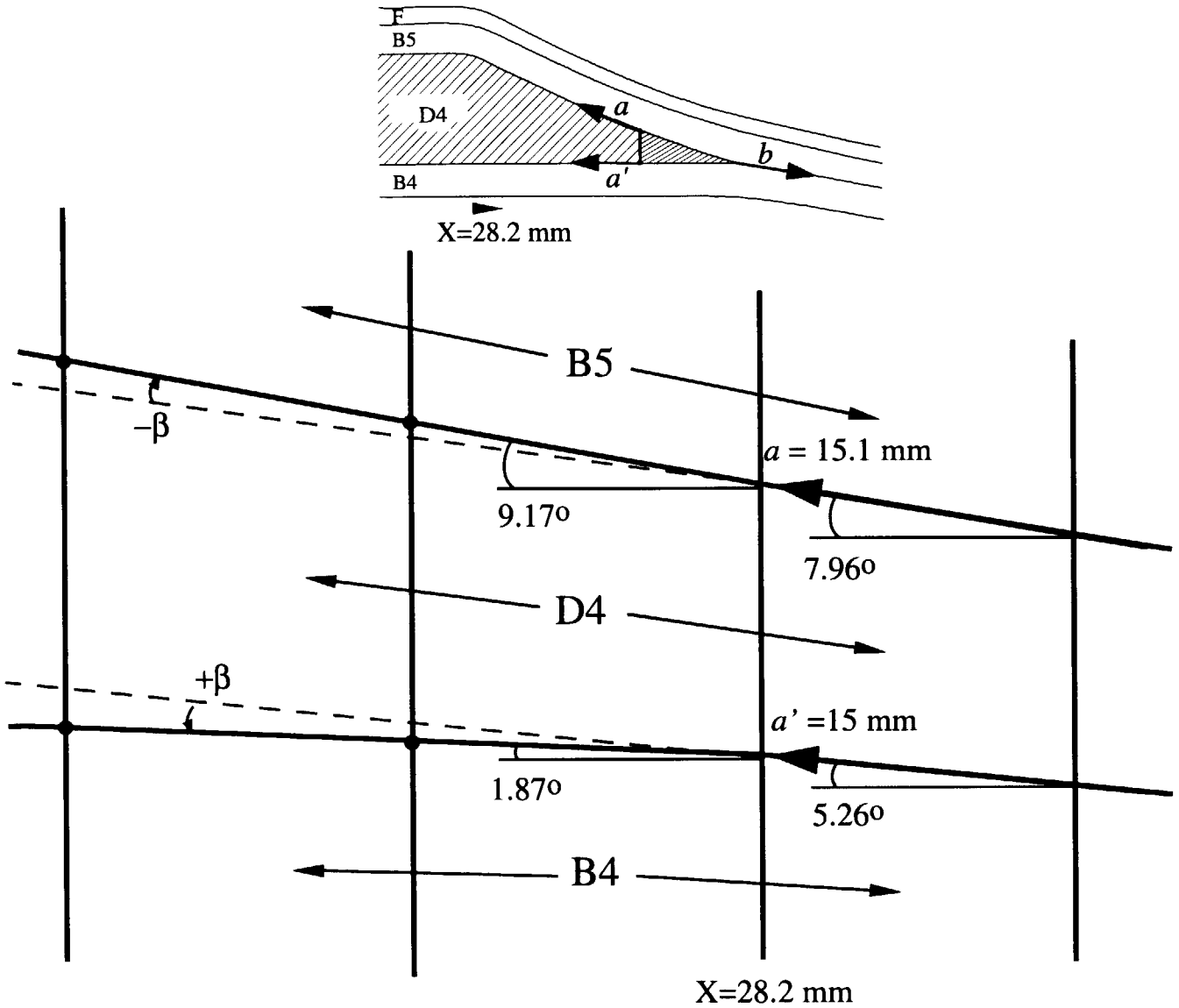

Figure 16. Mesh around X=28.19 mm showing taper angle changes.

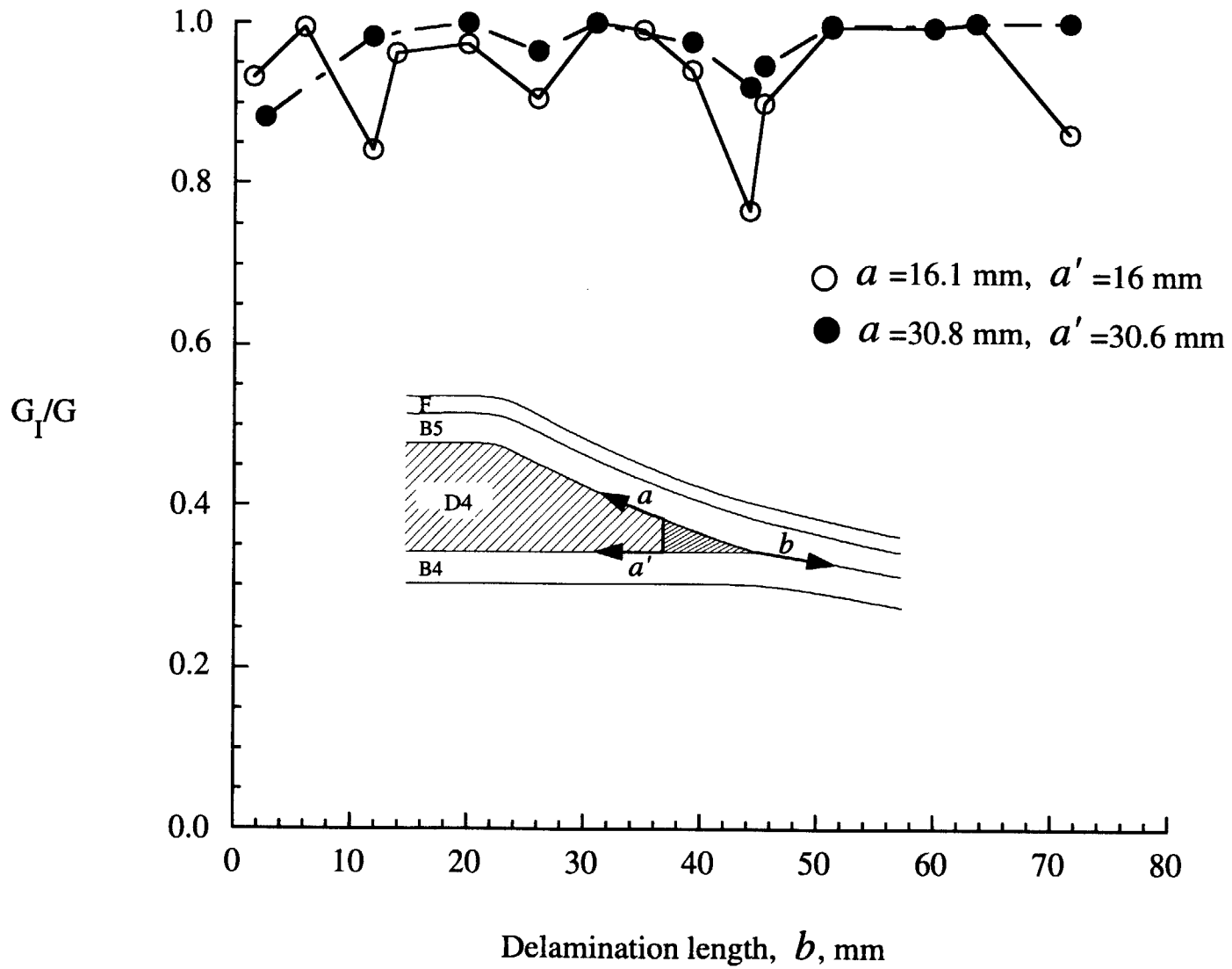

Figure 17. G_I/G ratio for delamination growth toward thin region of flexbeam.

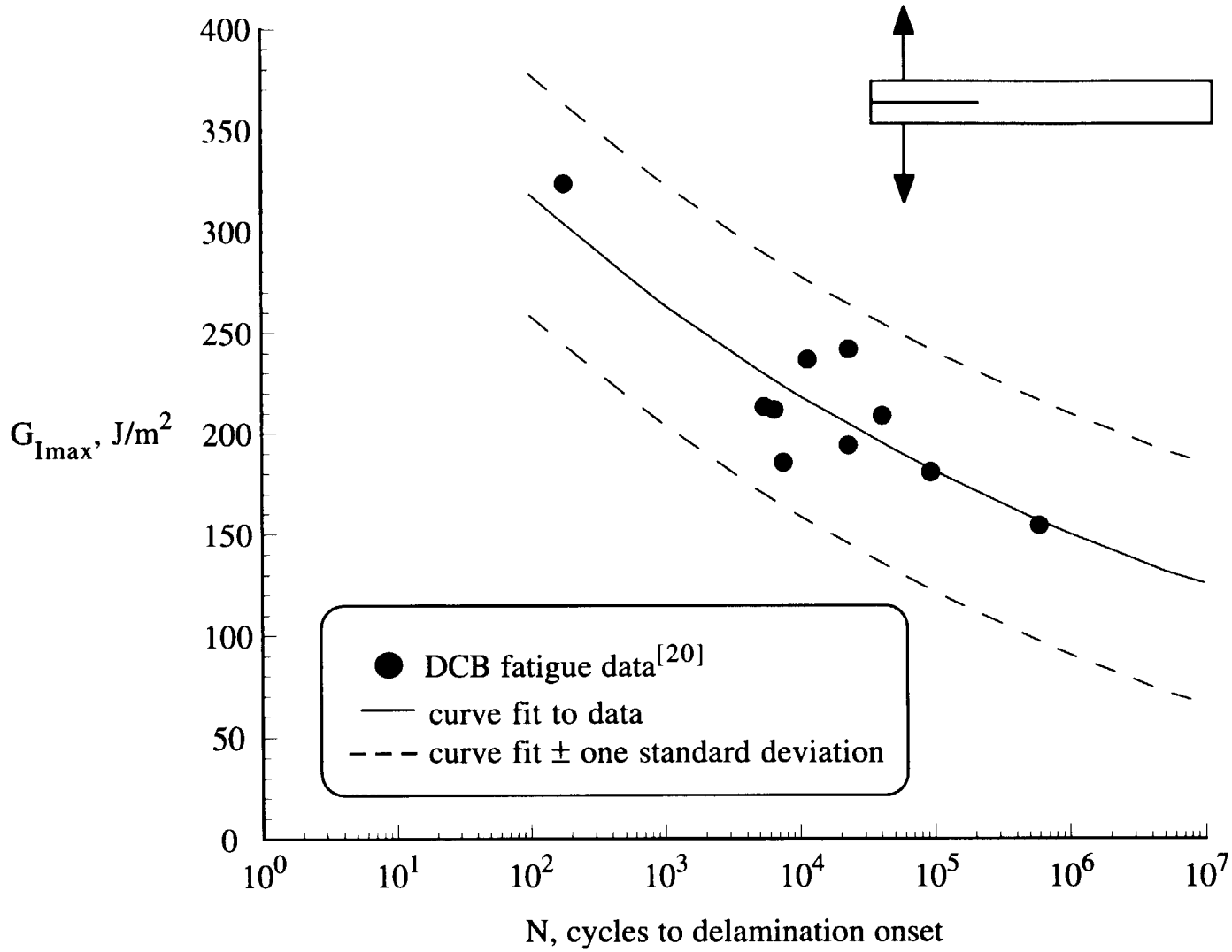

Figure 18. Fatigue delamination onset in S2/E7T1 DCB specimen.

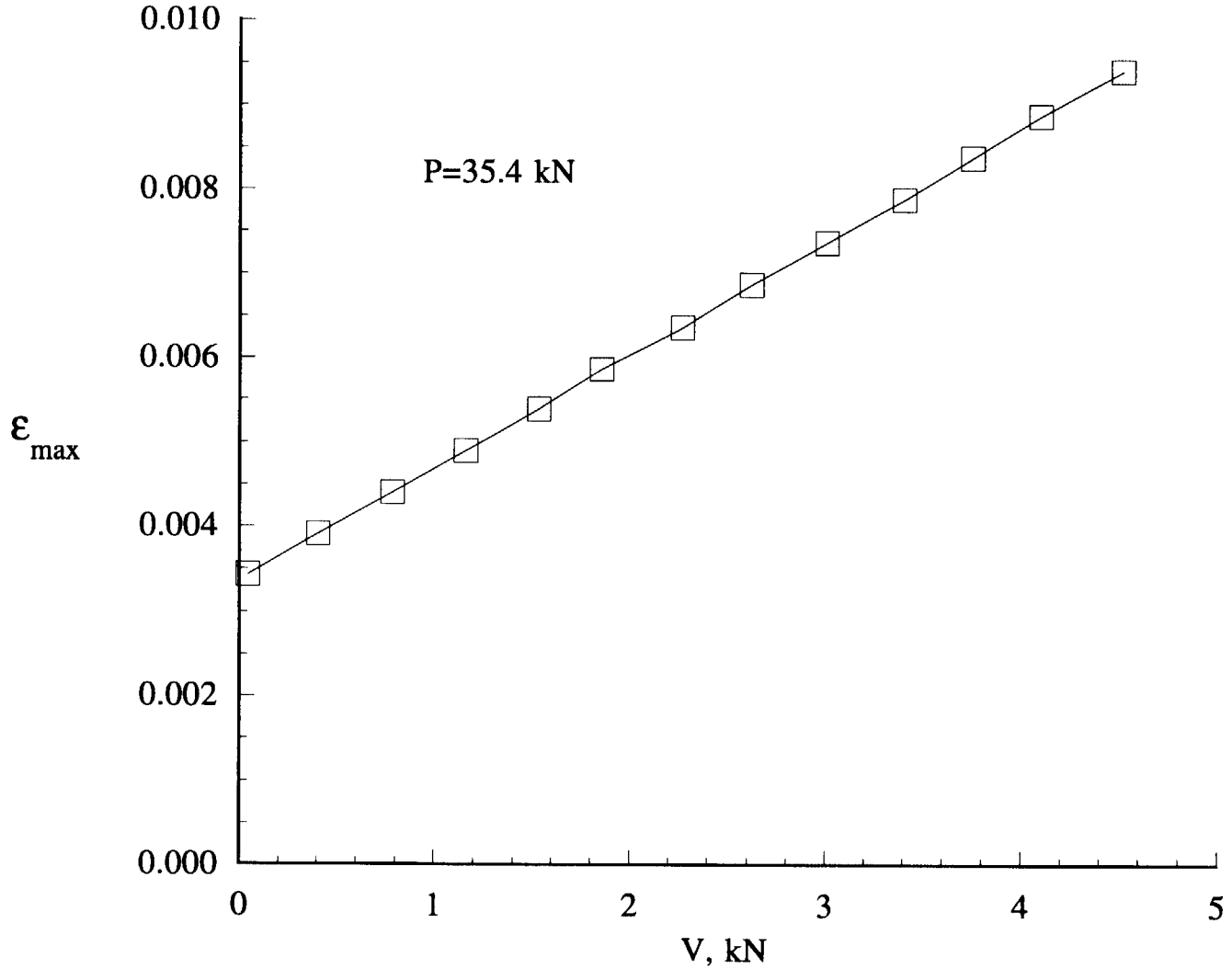

Figure 19. Maximum measured surface strain vs. applied transverse bending load in tapered flexbeam with constant axial tension load.

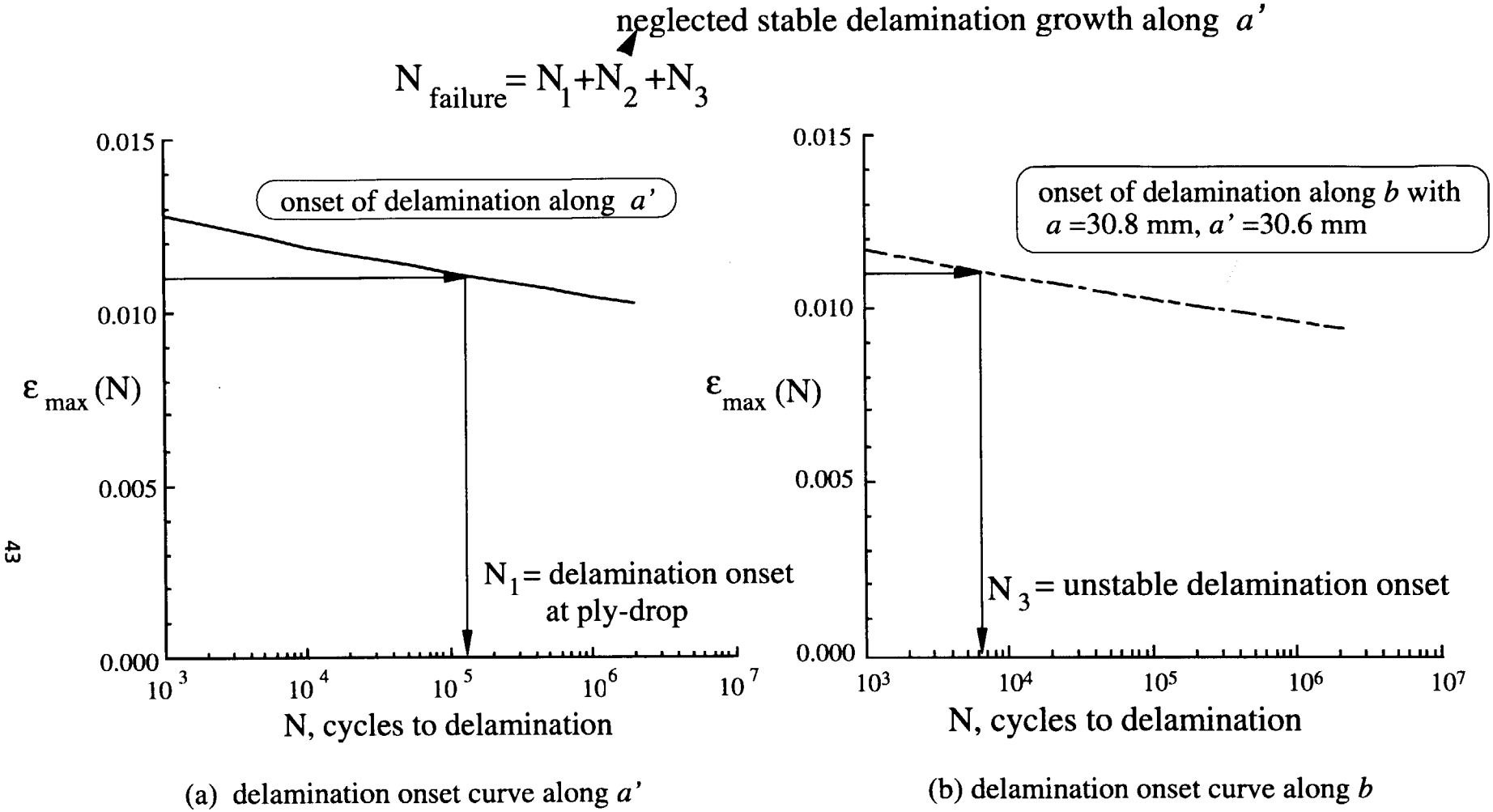

(a) delamination onset curve along *a'*

(b) delamination onset curve along *b*

Figure 20. Delamination onset curves for modeled delaminations.

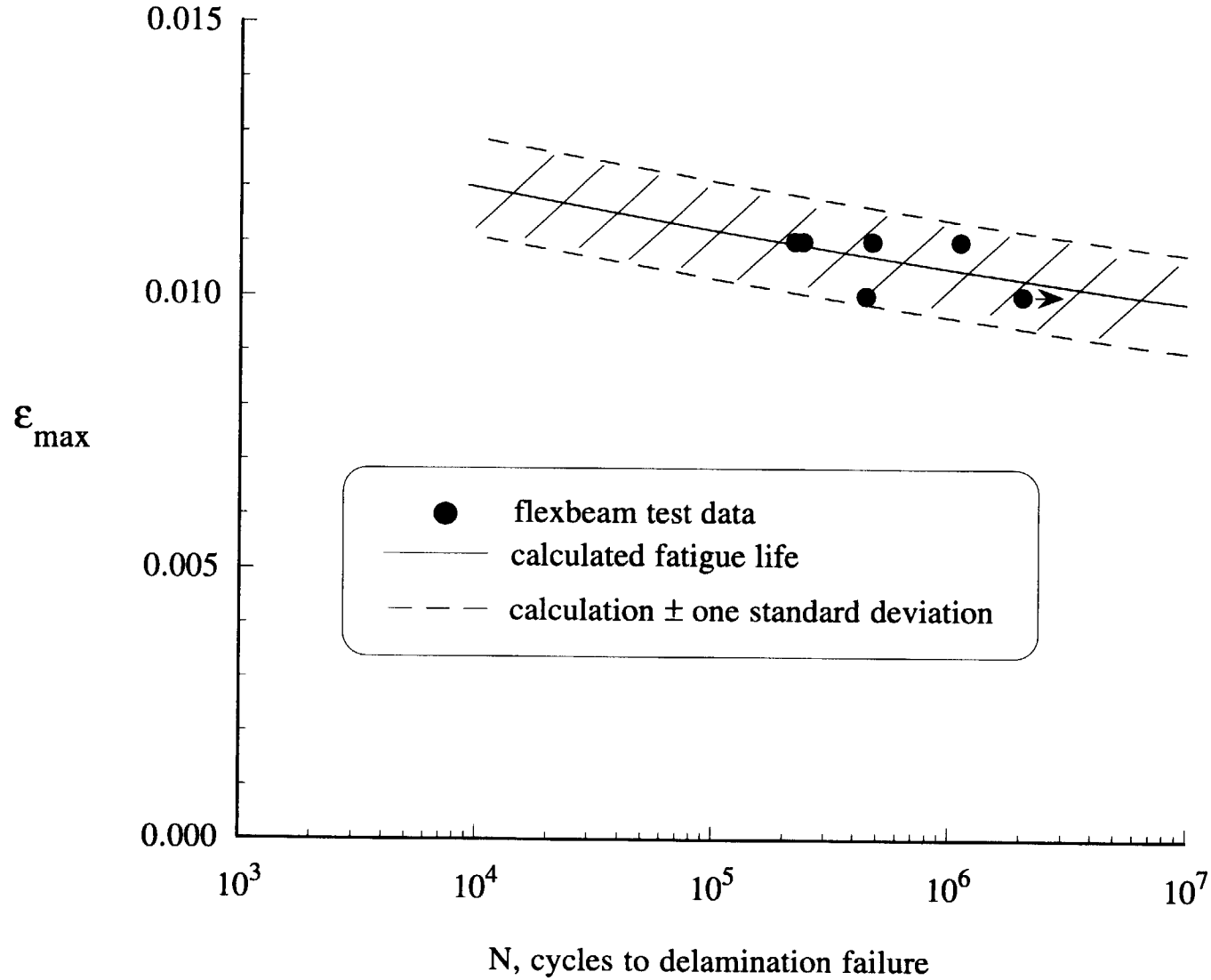

Figure 21. Flexbeam delamination failure data and calculated fatigue life curve.

REPORT DOCUMENTATION PAGE

Form Approved
OMB No. 0704-0188

1. AGENCY USE ONLY *(Leave blank)*	2. REPORT DATE	3. REPORT TYPE AND DATES COVERED
	May 1997	Technical Memorandum

4. TITLE AND SUBTITLE
Fatigue Life Methodology for Tapered Composite Flexbeam Laminates

5. FUNDING NUMBERS
WU 581-10-21-01

6. AUTHOR(S)
Gretchen B. Murri, T. Kevin O'Brien, and Carl Q. Rousseau

7. PERFORMING ORGANIZATION NAME(S) AND ADDRESS(ES)
NASA Langley Research Center
Hampton, VA 23681-0001 and
Vehicle Technology Center
U.S. Army Research Laboratory
NASA Langley Research Center, Hampton, VA 23681-0001

8. PERFORMING ORGANIZATION REPORT NUMBER

9. SPONSORING / MONITORING AGENCY NAME(S) AND ADDRESS(ES)
National Aeronautics and Space Administration
Washington, DC 20546-0001 and
U.S. Army Research Laboratory
Adelphi, MD 20783-1145

10. SPONSORING / MONITORING AGENCY REPORT NUMBER
NASA TM-112860
ARL-TR-1400

11. SUPPLEMENTARY NOTES
Murri: Langley Research Center, Hampton, VA; O'Brien: Langley Research Center, Hampton, VA; Rousseau: Bell Helicopter Textron, Ft. Worth, TX.

12a. DISTRIBUTION / AVAILABILITY STATEMENT
Unclassified - Unilimited

Subject Category 24

12b. DISTRIBUTION CODE

13. ABSTRACT ***(Maximum 200 words)***

The viability of a method for determining the fatigue life of composite rotor hub flexbeam laminates using delamination fatigue characterization data and a geometric non-linear finite element (FE) analysis was studied. Combined tension and bending loading was applied to nonlinear tapered flexbeam laminates with internal ply drops. These laminates, consisting of coupon specimens cut from a full-size S2/E7T1 glass-epoxy flexbeam were tested in a hydraulic load frame under combined axial-tension and transverse cyclic bending loads. The magnitude of the axial load remained constant and the direction of the load rotated with the specimen as the cyclic bending load was applied. The first delamination damage observed in the specimens occurred at the area around the tip of the outermost ply-drop group. Subsequently, unstable delamination occurred by complete delamination along the length of the specimen. Continued cycling resulted in multiple delaminations. A 2D finite element model of the flexbeam was developed and a geometrically non-linear analysis was performed. The global responses of the model and test specimens agreed very well in terms of the transverse flexbeam tip-displacement and flapping angle. The FE model was used to calculate strain energy release rates (G) for delaminations initiating at the tip of the outer ply-drop area and growing toward the thick or thin regions of the flexbeam, as was observed in the specimens. The delamination growth toward the thick region was primarily mode II, whereas delamination growth toward the thin region was almost completely mode I. Material characterization data from cyclic double-cantilevered beam tests was used with the peak calculated G values to generate a curve predicting fatigue failure by unstable delamination as a function of the number of loading cycles. The calculated fatigue lives compared well with the test data.

14. SUBJECT TERMS	15. NUMBER OF PAGES
flexbeam, delamination, tapered laminate, FEM, strain energy release rate	45
	16. PRICE CODE A03

17. SECURITY CLASSIFICATION OF REPORT	18. SECURITY CLASSIFICATION OF THIS PAGE	19. SECURITY CLASSIFICATION OF ABSTRACT	20. LIMITATION OF ABSTRACT
Unclassified	Unclassified		

NSN 7540-01-280-5500

Standard Form 298 (Rev. 2-89)
Prescribed by ANSI Std. Z39-18
298-102